Eidgenössische Technische Hochschule Zürich
Swiss Federal Institute of Technology Zurich

Ion-trap design for magnetic-field-driven quantum information processing

Roland Matt

Master Thesis

ETH Zurich

Supervisors:
Dr. Joseba Alonso
Prof. Jonathan Home

Department of Physics
Institute for Quantum Electronics
Trapped Ion Quantum Information group

Zurich, November 2016

Contents

Introduction **3**

1 Quantum logic gates based on oscillating magnetic fields **4**
- 1.1 Inhomogeneous magnetic field interacting with a qubit 5
- 1.2 Multiqubit gates 6
  - 1.2.1 Mølmer-Sørensen gate 6
  - 1.2.2 Implementing the $\hat{\sigma}_z\hat{\sigma}_z$ and $\hat{\sigma}_\varphi\hat{\sigma}_\varphi$ gates 7
  - 1.2.3 Dynamically-decoupled gate as an alternative to nulling B-field 8
  - 1.2.4 Gate times 9
- 1.3 Hyperfine qubit: ^{9}Be$^+$ ion 10

2 Design considerations for SETs with integrated microwave structures **11**
- 2.1 Basics of ion trapping 11
  - 2.1.1 A linear string of ions 12
  - 2.1.2 Surface-electrode Paul trap 13
- 2.2 SET geometries for magnetic-field-gradient gates 15
  - 2.2.1 Three parallel currents on a plane 16
  - 2.2.2 More complex models 17
  - 2.2.3 Three wires above a grounded plane 18
  - 2.2.4 Realizable geometries for the three-wire configuration 19
  - 2.2.5 Various electrode configurations 21
- 2.3 Scaling laws for surface traps 22

3 Superconducting Niobium thin films **23**

4 Ion traps for fast entangling microwave gates **26**
- 4.1 Design proposal 26
  - 4.1.1 Simulation results and settings 28
  - 4.1.2 3D meander 32
  - 4.1.3 Termination-tuned trident 35
- 4.2 Impedance matching 38
  - 4.2.1 Tuning the resonance frequency 41
- 4.3 Inter-electrode crosstalk 42

5 Individual ion addressing (IIA) **44**
- 5.1 Magnetic fields produced by IIA electrodes 46
- 5.2 IIA fidelity 47
  - 5.2.1 Gate time 48
- 5.3 Alternative uses of IIA electrodes 50

Summary and outlook **51**

Appendices **53**

Introduction

The amount of information contained in a quantum mechanical state is exponential in the number of basis states due to the possible quantum superpositions. This means, that computational power (time and memory) needed to simulate quantum systems grows exponentially with the system size (i.e. number of particles). This problem has fuelled the pursuit for an universal quantum computer which would make use of quantum mechanics [1]. Classical computers are compact and reliable due the implementation of various microfabrication technologies.

The logical information inside a quantum computer is contained in the physical states of quantum systems. The quantum analogue of an information bit is called a qubit. Today, quantum information has been encoded into many systems like nitrogen-vacancy-centers in diamonds [2], superconducting circuits [3], polarization states of photons [4] and trapped atomic ions. All of these systems can be compared on the basis the coherence time of the system and the interaction rate at which information can be written and read from the system. Quantum information processors based on trapped atomic ions are a promising candidate for realizing an universal quantum computer because the ions can be well isolated from the surrounding environment which provides qubits with very long lifetimes [5]. The Coulomb interaction provides a strong coupling between individual qubits. Information can be written by coupling to the ions electric or magnetic moments with strong electromagnetic fields produced by lasers or the near-fields of currents in electrodes [6, 7]. Current quantum information processing devices based on trapped ions [8] require multiple powerful laser sources with accompanying lenses and mirrors which impose increasing technical complications as systems grow larger. However, only a small number of trap designs [6, 9, 10, 11] and the first proof-of-principle type of experiments [12, 13, 14, 15, 16] have been realized with traps with integrated microwave (MW) near-field sources.

In this thesis, I present a study of a superconducting surface-electrode ion trap with integrated microwave structures for all-electronic coherent manipulations of trapped ions. This thesis has be structured into five chapters. Chapter 1 describes the interaction between an ion and a magnetic field. This is followed by discussing different entangling gate driving possibilities and finished by introducing the hyperfine $^{9}Be^{+}$ ion. Chapter 2 introduces surface-electrode ion traps (SETs) and discusses relevant design considerations for SETs with integrated microwave structures. The properties of thin superconducting Niobium sheets (Chapter 3) determine the current distribution in the electrodes. Chapter 4 discusses the simulation results for two different MW conductor geometries - the meander (proposed in Ref. [17]) and the trident (a novel design proposed in this thesis). The use of a resonator to build up the high currents required to drive fast gates has been studied. The possibilities of addressing ions individually with near-field MW fields are discussed in Chapter 5.

Chapter 1

Quantum logic gates based on oscillating magnetic fields

Trapped atomic ions are promising candidates for implementing scalable quantum computation. Internal electronic states can be used as quantum information carrying two-level systems called qubits. These can be coherently controlled using electromagnetic radiation in the optical or radio-frequency (RF) regime. Hyperfine ground-level atomic ("clock") levels have very long T_1 lifetimes, with transitions typically in the GHz regime which (at specific field values) are resilient to first-order Zeeman shifts caused by magnetic field fluctuations [10]. Entangling gates are necessary for universal quantum computation. These make use of entangling internal states of ions with their collective motional state. Coupling to the motional states makes also sideband cooling possible [18]. In order to couple the internal and motional degrees of freedom, the atom has to experience a spatial variation of the field that drives the internal transition. For free-field radiation, the relevant length scale over which the field value changes significantly is the wavelength λ. The characteristic size of an atom (its wave packet) with mass m trapped in a harmonic potential characterized by its angular frequency ω_j in the ground state is given by $\tilde{q}_0^j = \sqrt{\hbar/(2m\omega_j)}$. A measure for the strength of the field gradient relative to the atoms spacial extent is the Lamb-Dicke (LD) parameter $\eta = 2\pi\tilde{q}_0^j/\lambda$ [18]. This coupling can be reasonably strong for optical wavelengths but it is very weak for free-field microwave radiation[A]. However, it is possible to engineer trap structures which produce strong gradients of near-field microwaves [10, 11, 19, 20, 17]. In this case, the spatial variation of this radiation is dependent on the size scale of the electronics $\rho \ll \lambda$.

I will start by introducing a quantitative description of an inhomogeneous magnetic field interacting with a qubit in Section 1.1. This provides the groundwork for studying the possible entangling gates in the following Section 1.2. It will also motivate the effort to null magnetic fields by design. Section 1.2.3 introduces a method to circumvent complete field cancellation with a dynamically-decoupled gate scheme. Finally I will study the scaling of entangling gate time in Section 1.2.4 and describe $^9\mathrm{Be}^+$ as a candidate ion for experimental realization in Section 1.3.

[A] For $^9\mathrm{Be}^+$ and $\omega_j = 2\pi \times 5$ MHz we obtain $\Delta z \approx 10$ nm. The hyperfine transition $|S_{1/2}, F = 2, m_F = +1\rangle \to |S_{1/2}, F = 1, m_F = +1\rangle$, often used as a qubit because it is first-order magnetic field independent at 22.3 mT, has a transition frequency $\omega/2\pi = 1083$ MHz, which corresponds to $\lambda \approx 28$ cm [11]. This results in a Lamb-Dicke parameter $\eta \approx 2.2 \times 10^{-7}$.

1.1 Inhomogeneous magnetic field interacting with a qubit

In the following, I will present a short mathematical description of magnetic field interacting with an ion. This is based on work by C. Ospelkaus *et al.* [6].

Consider a string of N ions with mass m aligned along the x axis. Each ion has two relevant internal states $|\uparrow\rangle$ and $|\downarrow\rangle$ in the hyperfine manifold of the $S_{1/2}$ level. These can form a qubit with a transition frequency ω_0. Let there be a static magnetic field $B_0\vec{e}_y$ along the y axis which defines the quantization axis and let q_n be the displacement of the ion n relative to its equilibrium position $q_n = 0$. We can write q_n in terms of normal modes with coordinates $\tilde{q}_j$, amplitudes $b_{j,n}$ and frequencies ω_j

$$q_n = \sum_j b_{j,n}\tilde{q}_j \ . \tag{1.1}$$

From quantization we also have $\tilde{q}_j = \tilde{q}_0^j(\hat{a}_j + \hat{a}_j^\dagger)$ with $\tilde{q}_0^j = \sqrt{\hbar/(2m\omega_j)}$. Here $\hat{a}_j^\dagger$ and the $\hat{a}_j$ are the creation and annihilation operations for the normal motional modes respectively.

The interaction-free Hamiltonian for the qubit states and motion can be written as

$$\sum_n \frac{\hbar\omega_0}{2}\hat{\sigma}_z^n + \sum_j \hbar\omega_j\hat{a}_j^\dagger\hat{a}_j \ ,$$

where $\hat{\sigma}_z^n$ is the sigma z operator corresponding to the Pauli σ_z matrix measuring the qubit state of ion n.

Now we introduce an oscillating (with frequency ω and initial phase φ) magnetic field $\vec{B}(q,t)$ which will couple the internal state and motion. Expanding it to first order in terms of its projections on the Cartesian axis (defined by the unit vectors $\vec{e}_i$ where $i = x, y, z$). The time-dependent field components B_i are characterized with amplitudes $\tilde{B}_i$ and gradients $\tilde{B}_i'$:

$$\vec{B}(q,t) = \vec{e}_y B_y + \vec{e}_z B_z = \left[\vec{e}_y(\tilde{B}_y + q\tilde{B}_y') + \vec{e}_z(\tilde{B}_z + q\tilde{B}_z')\right] \times \cos(\omega t + \varphi) \ . \tag{1.2}$$

The interaction picture magnetic dipole Hamiltonian for ion n in the rotating-wave approximation (RWA) and in the LD regime is given by

$$\hat{H}_{I,n} = \hat{H}_{I,n}^B + \hat{H}_{I,n}^{B'} \ . \tag{1.3}$$

The global field (drive rate is independent of position) driven terms are

$$\hat{H}_{I,n}^B = -\hbar e^{-i(\omega t+\varphi)}(\Omega^y\hat{\sigma}_+^n e^{i\omega_0 t} + \Omega^z\hat{\sigma}_z^n) + \text{H.c.} \ , \tag{1.4}$$

where $\hat{\sigma}_+$ is the spin raising operator. The terms involving motional states (dependent on field gradient)

$$\hat{H}_{I,n}^{B'} = -\hbar e^{-i(\omega t+\varphi)}\left[\sum_j(\Omega_{j,n}^y\hat{\sigma}_+^n e^{i\omega_0 t} + \Omega_{j,n}^z\hat{\sigma}_z^n)(e^{i\omega_j t}\hat{a}_j^\dagger + e^{-i\omega_j t}\hat{a}_j)\right] + \text{H.c.} \ . \tag{1.5}$$

We will use to notation $\mu_{y\uparrow\downarrow} \equiv \langle\uparrow|\vec{\mu}|\downarrow\rangle$ for the matrix elements of the ion's magnetic moment $\vec{\mu}$. The Rabi frequencies in the above equations are:

- $\Omega^z = \frac{\tilde{B}_z}{4\hbar}(\mu_{z\uparrow\uparrow} - \mu_{z\downarrow\downarrow})$ describes the periodic change in the energy of each ion qubit due to the oscillating z component of the magnetic field.

- $\Omega^y = \frac{\tilde{B}_y}{2\hbar}\mu_{y\downarrow\uparrow}$ represents the driven Rabi oscillations applied to all ion-qubits simultaneously ("carrier" transitions) if the driving field frequency is close to ω_0.
- $\Omega^y_{j,n} = \frac{b_{j,n}\tilde{q}_0^j \tilde{B}'_y}{2\hbar}\mu_{y\uparrow\downarrow}$ describes spin-flip transitions ($\hat{\sigma}^n_+$) simultaneous with the creation or annihilation ($\hat{a}^\dagger_j,\ \hat{a}_j$) of phonons in motional mode j for $\omega \approx \omega_0 \pm \omega_j$.
- $\Omega^z_{j,n} = \frac{b_{j,n}\tilde{q}_0^j \tilde{B}'_z}{4\hbar}(\mu_{z\uparrow\uparrow} - \mu_{z\downarrow\downarrow})$ represents the qubit-state-dependent ($\hat{\sigma}^n_z$) excitations of motional mode j without simultaneous spin flips.

1.2 Multiqubit gates

Note that the Rabi frequencies $\Omega^{y,z}_{j,n}$ are gradient dependent and they represent simultaneous change rates in internal and motional states. Therefore, these can be used to implement multi-ion entangling gates. Usually field gradients are accompanied by non-zero field magnitudes. These will drive carrier transitions[B] and provide an AC Zeeman shift (with Rabi frequencies Ω^y and Ω^z respectively) which both lead to loss in two-qubit gate fidelities. A high gradient-to-field ratio is therefore required to realize high-fidelity entangling gates. Section 1.2.1 introduces the Mølmer-Sørensen gate, which is important for understanding the derivation of the entangling $\hat{\sigma}_\varphi\hat{\sigma}_\varphi$ gate in Section 1.2.2. In Section 1.2.3 I describe a dynamically-decoupled gate. This is one possibility to reduce the effect of the residual B-field magnitude.

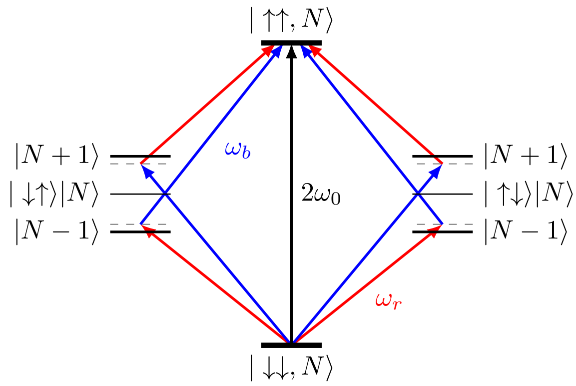

Figure 1.1: Entangling gate driving scheme. The idea is to apply two tones ω_r and ω_b detuned from single ion excitation ω_0 in such way that the two-photon process $|\downarrow\downarrow\rangle \rightarrow |\uparrow\uparrow\rangle$ is resonant. Here $|N\rangle$ represents the vibrational state of the ions motion with a quantum number N.

1.2.1 Mølmer-Sørensen gate

The two-qubit gates we will describe are very similar to the standard Mølmer-Sørensen (MS) gate [21]. It is implemented with a bichromatic field ($\omega_{b,r} = \omega_0 \pm \omega_j \mp \delta$) with frequencies slightly detuned (by δ) from the first blue and red sideband transitions ($\omega_{B,R} = \omega_0 \pm \omega_j$) of one of the ions' motional modes (see Fig. 1.1). The Hamiltonian which governs the dynamics is

$$\hat{H}_{\mathrm{MS}} = \frac{1}{2}\hbar\Omega\hat{S}\left(\hat{a}^\dagger_j e^{i\delta t} + \hat{a}_j e^{-i\delta t}\right) , \tag{1.6}$$

[B] Which will be off-resonant while driving side-bands but still significant.

where Ω is the Rabi frequency of the gate and $\hat{S} = \hat{\sigma}_x^{n=1} \pm \hat{\sigma}_x^{n=2}$ is the collective spin operator. The sign is positive (negative) when the ions' normal motions are in phase (anti-phase) with each other. The remarkable feature of the MS gate is that it is independent of the motional quantum number N, as long as we are in the LD regime [22].

1.2.2 Implementing the $\hat{\sigma}_z\hat{\sigma}_z$ and $\hat{\sigma}_\varphi\hat{\sigma}_\varphi$ gates

Ospelkaus *et al.* [6] introduce two possible entangling two-qubit gates. Firstly, the $\hat{\sigma}_z\hat{\sigma}_z$ gate which could be directly realized for magnetic field sensitive qubits at high radial frequencies. Secondly, the $\hat{\sigma}_\varphi\hat{\sigma}_\varphi$ gate which is an analogue to the Mølmer-Sørensen gate and could be implemented with atomic "clock" qubits at low radial frequencies.

Let us consider an oscillating B_z field at $\omega = \omega_j - \delta$ where δ is a small detuning. The relevant terms in the Hamiltonian are then [6]

$$\hat{H}_n^{zz} = -\hbar e^{i(-\omega_j+\delta)t} \left[\Omega^z \hat{\sigma}_z^n + \sum_j \Omega_{j,n}^z \hat{\sigma}_z^n (e^{-i\omega_j t}\hat{a}_j + e^{i\omega_j t}\hat{a}_j^\dagger) \right] + \text{H.c.} \tag{1.7}$$

$$= -\hbar e^{i\delta t} \Omega_{j,n}^z \hat{\sigma}_z^n \hat{a}_j + \text{H.c.}\ , \tag{1.8}$$

where in the last equality we have kept only resonant terms. This describes a spin-dependent periodic force under which the motional state of the ion follows a circular trajectory in the phase space. At $t = \tau = 2\pi/\delta$, the motional state has returned to the origin and the propagator is

$$\hat{U}_{zz}(\tau) = \exp\left[\frac{2\pi i}{\delta^2} \left(\sum_n \Omega_{j,n}^z \hat{\sigma}_z^n \right)^2 \right] . \tag{1.9}$$

As an example lets consider the two-ion "rocking" mode ($b_{j,1} = -b_{j,2} = b_j$)

$$\hat{U}_{zz} = \exp\left[\frac{2\pi i}{\delta^2} \frac{(b_j \tilde{q}_0^j \tilde{B}_z')^2}{16\hbar^2} (\hat{\sigma}_z^{n=1} - \hat{\sigma}_z^{n=2})^2 \right] . \tag{1.10}$$

From here we see, that taking $\delta/4 = \Omega_{j,n}^z$ we obtain a $\hat{\sigma}_z\hat{\sigma}_z$ gate as in Ref. [23]. The gate time is given by

$$\tau = \frac{2\pi}{\delta} = \frac{2\pi}{4\Omega_{j,n}^z} = \frac{2\pi\hbar}{b_{j,n}\tilde{q}_0^n \tilde{B}_z'(\mu_{z\uparrow\uparrow} - \mu_{z\downarrow\downarrow})} . \tag{1.11}$$

Note, that the $\sigma_z\sigma_z$ gate requires that $\mu_{z\uparrow\uparrow} \neq \mu_{z\downarrow\downarrow}$. In general this is not true for first order magnetic-field insensitive qubit states. However, using single-qubit rotations it is possible to temporarily transform from the field-independent qubit-state manifold and perform the gate.

For a $\hat{\sigma}_\varphi\hat{\sigma}_\varphi$ gate, the $\Omega_{j,n}^y$ term can be used to implement a type of Mølmer-Sørensen gate by simultaneously applying two B_y fields of equal amplitude at frequencies detuned from the first blue and red sideband by δ ($\omega_{b,r} = \omega_0 \pm \omega_j \mp \delta$) and with phases φ_b and φ_r respectively. After ignoring all but the resonant multiqubit spin-flip terms and waiting $\tau = 2\pi/\delta$, we get the propagator

$$\hat{U}_{\varphi\varphi}(\tau) = \exp\left[\frac{2\pi i}{\delta^2} \left(\sum_n \Omega_{j,n}^y \hat{\sigma}_{\varphi_s}^n \right)^2 \right] , \tag{1.12}$$

where $\varphi_s = (\varphi_b + \varphi_r)/2$. This propagator is equivalent to the $\hat{\sigma}_z\hat{\sigma}_z$ gate propagator.

1.2.3 Dynamically-decoupled gate as an alternative to nulling B-field

T. P. Harty *et al.* introduce a dynamically decoupled gate which stabilizes the qubit against a.c. Zeeman shifts and avoids the need to perfectly null microwave fields [15].

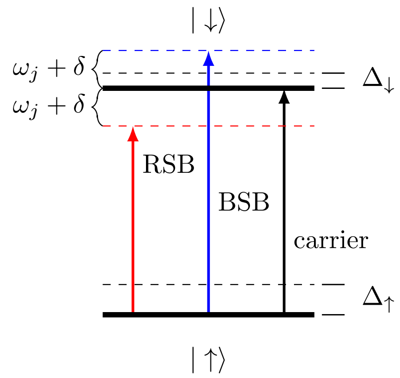

Figure 1.2: The dynamical decoupling scheme (not to scale). The strong sideband fields induce a differential a.c. Zeeman shift $\Delta = \Delta_\uparrow - \Delta_\downarrow$. The weak carrier field is tuned to resonance with the shifted qubit transition at $\omega_0 + \Delta$.

The differential a.c. Zeeman shift Δ on the qubit transition is induced by the fields which accompany the gradients that drive the ions motion. The shift of energy levels is described by the Hamiltonian

$$\hat{H}_Z = \frac{1}{2}\hbar\Delta\left(\hat{\sigma}_z^{n=1} + \hat{\sigma}_z^{n=2}\right) \ . \tag{1.13}$$

If Δ is constant then this may be compensated by adjusting the drive frequencies. Any fluctuations Δ' in Δ will lead to qubit dephasing, which can be a significant source for error. We now assume, that the bulk of Δ has been compensated for and only the slow fluctuation Δ' (relative to gate times) is present.

Since $\hat{H}_{\mathrm{MS}}$ does not commute with $\hat{H}_Z$ one can not use a spin-echo sequence. As $\hat{\sigma}_z$ gates require $\mu_{z\uparrow\uparrow} \neq \mu_{z\downarrow\downarrow}$ they are complicated to implement with microwaves on a hyperfine qubit. However, when the carrier phase is chosen correctly, it commutes with $\hat{H}_{\mathrm{MS}}$. The corresponding carrier drive (with Rabi frequency Ω_c) Hamiltonian is

$$\hat{H}_c = \frac{1}{2}\hbar\Omega_c\left(\hat{\sigma}_x^{n=1} + \hat{\sigma}_x^{n=2}\right) \ . \tag{1.14}$$

Going to the frame which rotates with the carrier drive yields the interaction picture Hamiltonian

$$\hat{H}_I = e^{i\frac{\hat{H}_c t}{\hbar}}(\hat{H}_{\mathrm{MS}} + \hat{H}_Z + \hat{H}_c)e^{-i\frac{\hat{H}_c t}{\hbar}} \tag{1.15a}$$

$$= \hat{H}_{\mathrm{MS}} + \frac{1}{2}\hbar\Delta' \sum_{n=1,2} \hat{\sigma}_z^k \cos(\Omega_c t) + \hat{\sigma}_y^k \sin(\Omega_c t) \ . \tag{1.15b}$$

If the additional carrier drive field is strong then $\Omega_c \gg \Omega, \Delta'$ and the summed terms in Eq.1.15 oscillate quickly and average out over the gate duration. This means, that the interaction frame Hamiltonian reduces to $\hat{H}_{\mathrm{MS}}$. To match the rotating frame to the lab frame at gate times t we need to tune the carrier field such that $\Omega_c t = 2m\pi$, where m is an integer.

1.2.4 Gate times

In this section, I will study the dependence of the MS gate time τ depending on the ion mass m, motional mode frequency ω_j and the trap RF frequency ω_{rf}. The scaling of the gate time depending on the trap size scale is presented in in Section 2.3. The Rabi frequency of the the entangling operation is given by

$$\Omega_{j,n} = \frac{b_{j,n}\tilde{q}_0^j \tilde{B}'_z \mu_{\uparrow\downarrow}}{2\hbar} \ . \tag{1.16}$$

The entangling gate is driven in

$$\tau \approx \frac{\pi}{2\Omega_{j,n}} \ . \tag{1.17}$$

We can simplify this expression using $\tilde{q}_0^j = \sqrt{\hbar/(2m\omega_j)}$, and writing $\mu_{\uparrow\downarrow} = \mu_B \bar{\mu}_{\uparrow\downarrow}$ where μ_B is the Bohr magneton and $b_{j,n} = [-1/\sqrt{2}, 1/\sqrt{2}]$ represent the transverse rocking mode [9]. After substitutions

$$\tau \approx \frac{2\pi\sqrt{\hbar}}{\mu_B} \times \frac{\sqrt{m\omega_j}}{\tilde{B}'_z \bar{\mu}_{\uparrow\downarrow}} \tag{1.18}$$

where I have separated the universal constants and experimentally controllable quantities. For a pair of $^{25}\mathrm{Mg}^+$ driven on a 7.6 MHz transverse rocking mode, as in Ref. [12], we get $\tau = (\tilde{B}'_z \bar{\mu}_{\uparrow\downarrow})^{-1} \times 9.8$ ms. The field gradient in [12] was 35.3 T/m, leading to $\tau \approx 0.25$ ms.

The reduced matrix elements of the magnetic moment for $^{43}\mathrm{Ca}^+$ ion have been listed in Ref. [9]. I will use $\bar{\mu}_{\uparrow\downarrow} \approx 1$ for estimations for the $^{9}\mathrm{Be}^+$ ion.

1.3 Hyperfine qubit: $^9Be^+$ ion

In order to carry out quantum logic experiments driven by magnetic field we require qubit transitions in the microwave regime. Hyperfine levels in the ground states of ions fill this requirement[C]. As an additional advantage, these levels can have first order magnetic-field-independent ("clock") transitions. These transitions have very long lifetimes (seconds) and are resilient to magnetic field noise - an important source of decoherence [5]. A thorough analysis of the hyperfine ground level qubits has been written by Allcock in Ref. [9, p. 90]. In this section I will introduce features of a hyperfine qubit using $^9Be^+$ as an example.

The $^9Be^+$ ion is the lightest ion species commonly trapped in quantum information experiments. Due to its small mass it experiences strong confinement in the trap which results in high oscillation frequencies. The coupling between the orbital angular momentum $\vec{L}$ of the outer electron and its spin angular momentum S produces the fine structure of energy levels. The coupling of total electronic angular momentum $\vec{J} = \vec{L} + \vec{S}$ to the nuclear spin $I = 3/2$ creates the hyperfine splitting into states with a total angular momentum given by $\vec{F} = \vec{J} + \vec{I}$. The hyperfine manifolds (where $F = const.$) are split by the magnetic field and degenerate when the field is zero. The separation of the $F = 1$ and $F = 2$ at zero field is 1.25 GHz. There exist two pairs of levels in the $S_{1/2}$ ground state which at certain magnetic field values form a first-order magnetic field-independent transition. These are $|F = 1, m_F = 1\rangle \rightarrow |2, 0\rangle$ (at 1.207 GHz, $B_0 = 11.9$ mT) and $|1, 1\rangle \rightarrow |2, 1\rangle$ (at 1.083 GHz, $B_0 = 22.3$ mT) [24]. The electric-dipole selection rules determine the dipole-allowed transitions and also set the requirements for the polarization of radiation which can be absorbed by the ion. Transitions with a change in angular momentum $\Delta m = \pm 1$ can be excited with radiation with $\sigma^{\pm}$ polarization. Transitions with $\Delta m = 0$ can be excited with linearly polarized radiation [25]. Because linearly polarized near-fields are technically easier to realize [17] I focus here on the $|1, 1\rangle \rightarrow |2, 1\rangle$ transition.

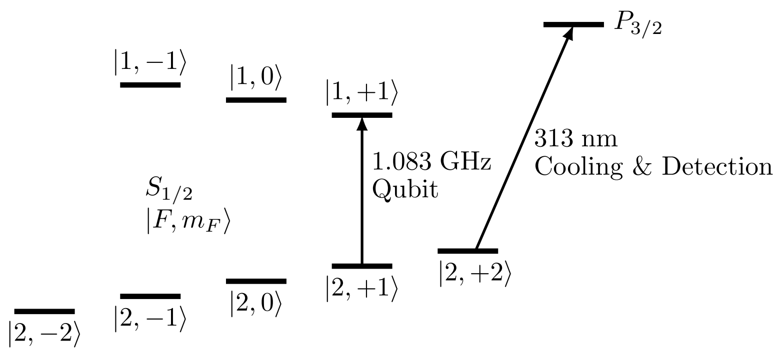

Figure 1.3: Hyperfine structure of $^9Be^+$ at 22.3mT. The transition $|2, +1\rangle \rightarrow |1, +1\rangle$ forms a first order magnetic field independent qubit [11]. The 313 nm optical transition can be used for Doppler cooling and read-out.

[C]The hyperfine splitting is magnetic-field-dependent.

Chapter 2

Design considerations for SETs with integrated microwave structures

The purpose of ion trapping for quantum information processing is to confine individual charged particles for coherent manipulations of their quantum states. The ions have to be well isolated from any noise of the surrounding environment but be accessible for strong controlled interactions. This chapter introduces design considerations for realizing coherent quantum control of trapped ions by using microwave frequency (MW) magnetic near-fields. I will start with a brief introduction to ion-trap physics and introduce some relevant concepts in Sec. 2.1. This is followed by defining important design considerations for realizing a surface-electrode ion-trap which employs oscillating magnetic near fields for quantum control (Sec. 2.2). In the last section I derive a set of scaling laws for a qualitative understanding of how gate times and infidelity caused by stray fields depend on trap size.

2.1 Basics of ion trapping

The Laplace equation prohibits the confinement of charged particles in free space by static electric fields[A]. This problem can be circumvented by using a combination of static and oscillating electric fields. The Paul trap [26] uses a radio-frequency (RF) quadrupole field and a static electric field to confine charged particles. This field configuration forms a three dimensional confining potential when the RF oscillation is much faster than the ions' motional frequencies in the trap. Paul traps are valuable for quantum-information-processing (QIP) experiments because the localized harmonic motion can be cooled to the quantum regime and controlled relatively easily.

Surface fabrication methods facilitate scalability, which is important for QIP. This has motivated the development of planar Paul traps [27]. The first stable confinement of atomic ions in a surface electrode Paul trap (SET) was achieved at 2006 by S. Seidelin *et al.* [28]. In a SET, the ion experiences larger field gradients because it is being held closer to trapping electrodes[B]. This is useful as it allows faster transport,

[A]This is known as *Earnshaw's theorem.*

[B]The "traditional" Paul trap has a three-dimensional geometry where the typical electrode-ion distance is hundreds of microns. Typical electrode-ion distances used at surface electrode traps range between $30 - 100$ μm. Operating small traps is challenging due to heating caused by surface effects better control over ions motion and the use of near-fields for local operations.

For our design, we have chosen the symmetric "five wire" geometry proposed by Chiaverini *et al.* in Ref. [27] (see Fig. 2.1). A RF potential is applied to two electrodes (of equal width), separated and surrounded by RF-grounded electrodes parallel to the trap axis. The symmetry of the electrode arrangement simplifies the design and optimization by reducing the number of parameters. Furthermore, a symmetric configuration of electrodes (with respect to the trap axis) naturally simplifies achieving the necessary conditions for realizing magnetic-field-driven gates in several aspects.

A thorough treatment of ions' motion in a Paul trap can be found in Ref. [29, Chap. 2]. I will introduce the most important conclusions which are crucial for a basic understanding of ion trapping in the following.

The electric potential at the position of the ion $\vec{r}$ is assumed to be quadratic to first order

$$\Phi(r,t) = \frac{1}{2}\sum_i u_i r_i^2 + \frac{1}{2}\sum_i v_i r_i^2 \cos(\omega_{\mathrm{rf}} t) \ . \tag{2.1}$$

This determines the motion of the ions' center of mass around the trap center ($\vec{r} = 0$) in Cartesian coordinates $i = x, y, z$. The curvatures u_i and v_i are proportional to the voltages applied ($u_i \propto V_{\mathrm{dc}}$,$v_i \propto V_{\mathrm{rf}}$) on the electrodes and depend on the trap geometry. The curvatures scale as $1/\rho^2$, where ρ is the size scale of the trap. In our case, the static confinement will be along the x direction (*axial confinement*) and the oscillating field at frequency ω_{rf} provides the confinement in the y and z (*radial*) directions. The Newtonian equation of motion is therefore

$$\frac{d^2 r_i}{dt^2} = -\frac{e}{m}\frac{\partial \Phi}{\partial r_i} = -\frac{e}{m}\left(u_i r_i + v_i r_i \cos(\omega_{\mathrm{rf}} t)\right) \ . \tag{2.2}$$

This can be written in terms of dimensionless parameters

$$\frac{d^2 r_i}{d\tau^2} + (a_i - 2q_i \cos(2\tau)) r_i = 0 \ , \tag{2.3}$$

which is called the Mathieu equation [29]. The parameter $\tau = \omega_{\mathrm{rf}} t/2 + \pi/2$ can be interpreted as a normalized time, $a_i = 4eu_i/m\omega_{\mathrm{rf}}^2$ and $q_i = 2ev_i/m\omega_{\mathrm{rf}}^2$ determine the trap stability and describe the axial and radial confinement respectively.[C] These parameters are important as they define a regime where the motion of the ion is harmonic to first order in all three axes, called the *pseudopotential approximation*. For this a and q must satisfy

$$|a_i| \ll q_i^2 \ll 1 \ . \tag{2.4}$$

If this condition is true, the harmonic motion in the radial direction is described by the oscillation frequency $\omega_i = \beta_i \omega_{\mathrm{rf}}/2$ where $\beta_i \approx \sqrt{a_i + q_i^2/2}$. We come to the expression $\omega_i \approx q_i \omega_{\mathrm{rf}}/2\sqrt{2} = ev_i/\sqrt{2} m\omega_{\mathrm{rf}}$ using $\beta_i \approx q_i/\sqrt{2}$. The analytic form for the curvature of the pseudopotential can be derived by viewing the RF field acting on the ion as a ponderomotive force. A crude derivation is presented in Appendix 5.3.

2.1.1 A linear string of ions

Microwave near-field driven entangling gates rely on the ions' shared modes of motion (see Sec. 1.1). For this reason, it would be useful to have the ions in the same potential well for entangling operations. On the other hand, the fidelity of individual ion addressing increases with ion-ion distance $d_{\text{i-i}}$ because of reduced crosstalk between the addressing regions. The goal is to design a geometry where both entangling gates

and limited laser access.

[C] Parameters a and q are typically much smaller than one. For the TIQI group cryogenic SET $a \leq 0.0005$ and $q \leq 0.15$ [29].

and individual operations could be driven with high fidelity. If the fields used for individual ion addressing can not be localized to the $d_{\text{i-i}}$ scale then the ion string has to be split into two independent wells and separated by transport before any individual addressing operation. This would be best avoided as separation, transport and recombination increase operation times and cause motional heating.

If several ions are trapped in the same axial harmonic well then they form an ion string when the radial confinement is sufficiently strong. The separations between the ions is determined by the Coulomb repulsion and the strength of the axial confinement. Maintaining the linear configuration is important to avoid heating due to *excess micromotion* (see Section 2.1.2) that the ion experiences when placed off the pseudopotential null. The ion string containing N identical ions forms a stable string if the frequencies ω_r and ω_x satisfy

$$\frac{\omega_{\text{r}}}{\omega_{\text{x}}} > 0.73N^{0.86} \,. \tag{2.5}$$

The stable mean distance for two ions in the trap is [30]

$$d_{\text{i-i}} \approx 2^{0.43} \left(\frac{e^2}{4\pi\epsilon_0 m\omega_{\text{x}}^2} \right)^{1/3} \,. \tag{2.6}$$

For two $^9\text{Be}^+$ ions $d \approx 9.86 f_x^{-2/3}$ µm when $f_x = \omega_x/2\pi$ is measured in MHz. Axial frequencies 1 MHz and 5 MHz correspond 9.86 µm and a 3.38 µm separations respectively. Another possibility would be to use smaller trap structures and lower trapping heights. However, heating rates may become a limiting factor on how low the axial frequencies and trapping position can be made [31].

2.1.2 Surface-electrode Paul trap

In the following I will introduce some important concepts for surface-electrode traps. The trap design proposed in this thesis is a symmetric *five-wire trap* where the electrodes between the RF lines are used for producing MW near-fields for gate operations. Our goal is to drive high fidelity quantum gates fast. A symmetric design helps to minimize *intrinsic micromotion* [31] which leads to *motional heating of the ion.* Minimizing the ions' motional heating leads to high fidelity operations. Gate operations can be made faster by bringing the ion closer to the electrode surface and driving high-power MW currents through the trap structures. However, these surfaces are a source of electric field noise which leads to incoherent excitations of the ions' motional modes. *Electrical heating of the trap* during gate operations leads to partial loss of control over the operation as trap properties are temperature dependent. The following Subsections will further explain these issues.

A five-wire SET

Figure 2.1 illustrates the electric field and potential in the radial plane of an asymmetric[D] five-wire surface-electrode Paul trap. The red dot represents the position of an ion. If the RF electric field at that position is not zero or the ion is not positioned at the pseudopotential null then the ion will experience an electric field oscillating at ω_{rf}.

The eigenaxes of an ion's radial motion determine the direction of the cooling laser. The orientation of the eigenaxis is determined by the (a)symmetry properties of the RF electrodes and the voltages applied by the DC electrodes. To cool the ion's motion on both radial modes, the wave vector of the cooling laser must have a non-zero projection on both of the modes. For the asymmetric configuration the eigenaxis

[D] The RF electrodes do not have equal width.

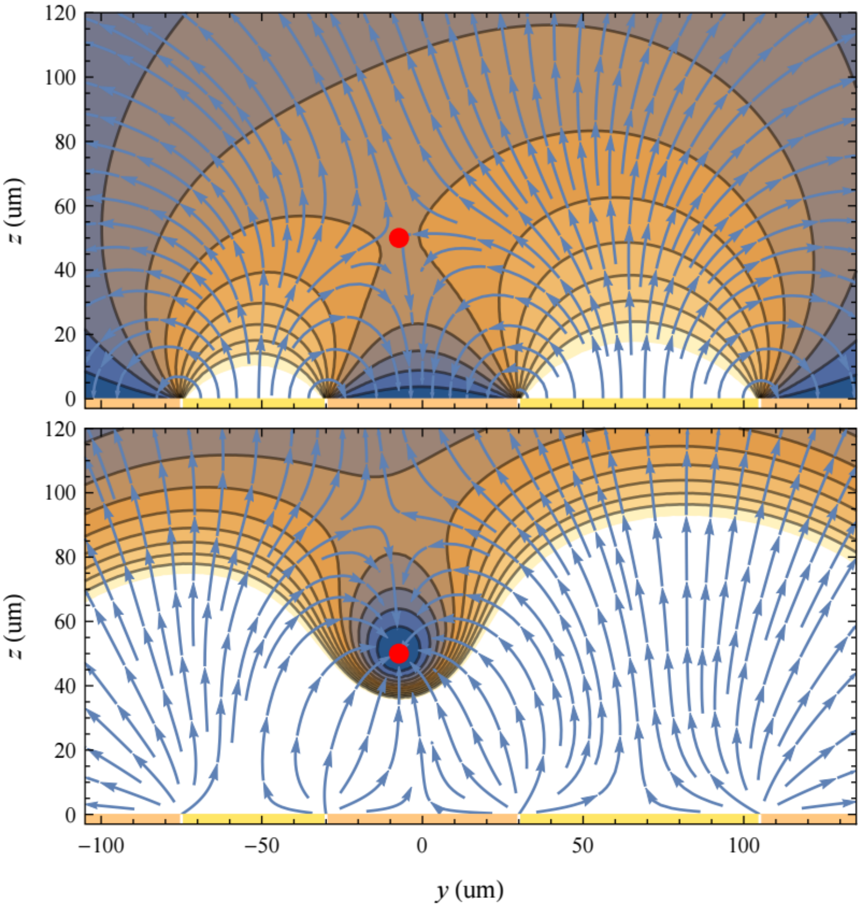

Figure 2.1: This is an example of electric potential and field lines above an asymmetric five-wire surface electrode Paul trap. (top) Instantaneous electric potential and field in the $x = 0$ plane. (bottom) The pseudopotential has a minimum (red dot) where the instantaneous field has a saddle point. This is point where the ion will be trapped. The oscillating electric fields are produced by the two electrodes (shown in yellow) separated by ground electrodes (brown). Figure taken from [29, p. 13].

of the radial modes are “tilted” (not parallel) with respect to the trap surface normal, which makes cooling both radial modes with a single beam (which is parallel to the trap surface) possible. The symmetric setup introduces the difficulty of cooling one of the radial modes of motion. It has been shown that additional DC potentials can be used to rotate the motional eigenaxis such that laser cooling on all modes is possible [9, p. 42].

As a potential benefit for scaling, it was noted by J. Kim *et al.* [32] that microelectronics for control of electrode potentials could be fabricated below the trap surface – this project will make use of subsurface ground layers and waveguides for shielding, routing signals and impedance matching with on-chip capacitors. On-chip resistors could be used to engineer electric losses to further improve impedance matching, realize filters, etc.

Micromotion

It is possible, that the pseudopotential at the equilibrium position of the trapped ion is not zero. This causes the ion to oscillate at the frequency ω_{rf}. Micromotion caused by the asymmetry/complex geometry of the trap is called *intrinsic* micromotion. A static electric field at the position of the pseudopotential null causes the equilibrium position of the ion to shift. This is called *excess* micromotion since potentials on shim (peripheral) DC electrodes can be applied to null these fields. Intrinsic micromotion can be caused by RF phase differences between both electrodes, which can be due to path length differences or a differential coupling to the ground [31]. Therefore a symmetric design helps to minimize intrinsic micromotion.

Motional heating of the ion

Electric field fluctuations couple to the ions' motional modes leading to incoherent heating of the motion, which can reduce the fidelity of coherent operations. This field noise can originate from stray charges gathered on exposed dielectric surface [33].

Electrical heating of the trap

When a traps' temperature changes, also its electrical properties change. This can lead to infidelities in control and even to trap breakdown. All conducting materials dissipate heat due to electric resistance, and all dielectrics dissipate the energy of alternating fields. The size of the trap components, the heat capacity and conductivity of the materials determine the rate at which these changes happen. To achieve stable trapping conditions, it is important to use materials with high thermal and electric conductivity and dielectrics with low loss tangents. We propose the use of superconducting Nb for maintaining high currents and achieving good shielding at MW frequencies.

2.2 SET geometries for magnetic-field-gradient gates

In order to realize a SET with the possibility to drive microwave quantum logic gates some electrodes need to carry MW frequency current. This can be realized by adding new electrodes or running microwave currents through existing electrodes. Both methods introduce new constraints on the usable geometries and technologies. In the following we will mainly stress design considerations for driving magnetic-gradient entangling gates. For this we need to generate high magnetic field gradients and low field values on a long section of the trap axis, like suggested in Ref. [6]. When designing a suitable geometry for driving microwave-gradient gates, the considerations listed below have to be taken into account

- it must be possible to trap a string of ions very close to the magnetic near-field minimum[E];
- microwave electrodes should be as close to the ion as possible to realize maximal gradient per unit current;
- it is important to have a small number of electrodes which need phase and amplitude control, for better scalability and control;
- microwave electrodes should be designed to carry as much current as possible (turns and vias are critical points which require extra attention);
- minimizing input losses can be done by using resonant structures and impedance matching;

[E] An ion experiences excess micromotion if it is not at the pseudopotential null and it experiences a non-zero oscillating magnetic field (which drives the carrier transition) if it is not placed at the center of the magnetic field quadrupole.

I have chosen to pursue the use of small electrodes for providing individual addressing conditions using microwave fields. A combination of small current carrying electrodes can create magnetic fields which vary spatially in the length scale of the electrodes [10]. Other solutions based on near-field effects rely on creating strong static field gradients along the trap axis. This was suggested in Ref. [18] and realized with a complicated surface electrode structure in Ref. [34]. The idea relies on spatially varying Zeeman splitting.

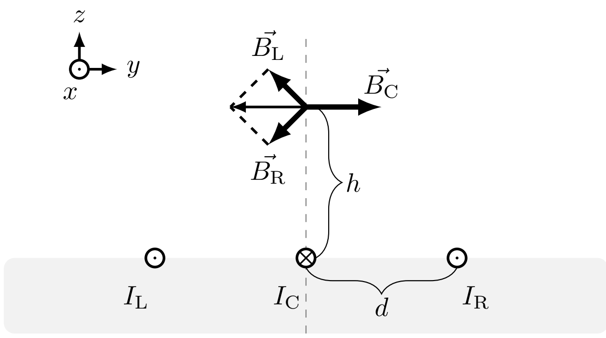

Figure 2.2: The magnetic fields produced by the three individual wires. The wires are parallel but the center current I_{C} is anti-parallel to I_{L} and I_{R}. At certain current amplitude and phase settings, a magnetic field null can be created on the symmetry axis.

2.2.1 Three parallel currents on a plane

Using three parallel currents which sit on the same plane is the simplest current configuration to realize a quadrupole field configuration outside the plane of the wires. The magnetic field amplitude vanishes at the center of the quadrupole but a considerable field gradient remains. This position can be used to drive the entangling gate [6]. I will now present a simplified model assuming infinite thin wires and discuss the effect of various simplifications. Fig. 2.2 describes the fields from three wires which cancel at a certain height h above the plane of the wires. This happens on the symmetry axis of the system only if $I_{\mathrm{L}} = I_{\mathrm{R}}$ and $\vec{B}_{\mathrm{L}} + \vec{B}_{\mathrm{R}} + \vec{B}_{\mathrm{C}} = \vec{B}_{\mathrm{S}} = \vec{0}$. The gradient $\nabla\vec{B}_{\mathrm{S}}$ at this point of interest can be found as the superposition ($\nabla\vec{B}_{\mathrm{S}} = \nabla\vec{B}_{\mathrm{L}} + \nabla\vec{B}_{\mathrm{C}} + \nabla\vec{B}_{\mathrm{R}}$) of gradients produced by the three individual wires.

Firstly, I will calculate the relation between the magnetic field minimum height h as a function of $I_{\mathrm{L}} = I_{\mathrm{R}} = I_{\mathrm{S}}$, I_{C} and d assuming that all the currents are in phase. The spacing between the wires is d. If each wire has length $l \ll \lambda$ much smaller than the free space wavelength of the microwave field, the field B_l can be integrated over the length of the wire assuming a constant current. The field produced at distance r from the center of a straight thin wire is

$$B_{\mathrm{l}} = \frac{I\mu_0}{2\pi r} \times \frac{l/2}{\sqrt{(l/2)^2 + r^2}} , \tag{2.7}$$

where I have expressed the field as a multiplication of the field magnitude produced by an infinite wire and a geometric factor originating from finite length. In the following analytic derivations I will ignore the geometric factor to arrive to analytic results. However, length dependence will be taken into account when numerically solving a more accurate analytic model (see Subsec. 2.2.3). Solving for the magnetic field minimum height

$$|\vec{B_\mathrm{C}}| = |\vec{B_\mathrm{L}} + \vec{B_\mathrm{L}}| = \tag{2.8a}$$

$$\frac{I_\mathrm{C}\mu_0}{2\pi h} = 2\frac{I_\mathrm{Side}\mu_0}{2\pi\sqrt{h^2+d^2}}\frac{h}{\sqrt{h^2+d^2}} \rightarrow \tag{2.8b}$$

$$h = \pm d\frac{\sqrt{I_\mathrm{C}}}{\sqrt{2I_\mathrm{Side} - I_\mathrm{C}}} \tag{2.8c}$$

which in case of $I_\mathrm{C} = I_\mathrm{L} = I_\mathrm{R}$ yields $|h| = d$. This result shows that controlling the $I_\mathrm{C}/I_\mathrm{Side}$ shifts the position of the minimum.

Let us now calculate the field gradient at the point of interest. We are interested in the gradient magnitude of the y-component of the magnetic field because this will drive the entangling gate 1.2.2. This gradient (on the symmetry axis) is parallel to z-axis. Other gradient components are zeros due to the symmetry of the field. I will now derive an expression for the gradient $\partial B_y/\partial z$ of a finite wire with length l at position $y = d$. The magnitude of B_y is

$$B_y = \frac{I\mu_0}{2\pi\sqrt{h^2+y^2}}\frac{l/2}{\sqrt{(l/2)^2+h^2+y^2}}\frac{h}{\sqrt{h^2+y^2}}\ . \tag{2.9}$$

Using $r = \sqrt{h^2+y^2}$, the z-component of the gradient is

$$\frac{\partial B_y}{\partial h}(I,d) = \frac{-I\mu_0 l}{2\pi r^2\sqrt{\left(\frac{l}{2}\right)^2+r^2}}\left[\frac{1}{2} - \frac{h^2}{r^2} - \frac{h^2}{2\left(\left(\frac{l}{2}\right)^2+r^2\right)}\right]\ . \tag{2.10}$$

We now add up the gradients of the three wires

$$|\nabla\vec{B}| = |\nabla\vec{B_\mathrm{L}} + \nabla\vec{B_\mathrm{C}} + \nabla\vec{B_\mathrm{R}}|\ , \tag{2.11a}$$

$$= \left.\frac{\partial B_y}{\partial h}\right|_{I=I_\mathrm{C},y=0} + \left.\frac{\partial B_y}{\partial h}\right|_{I=-I_\mathrm{Side},y=-d} + \left.\frac{\partial B_y}{\partial h}\right|_{I=-I_\mathrm{Side},y=d}\ . \tag{2.11b}$$

$$\tag{2.11c}$$

Taking $I_\mathrm{C} = I_\mathrm{Side} = 1$ A, $l = 200$ µm and $h = d = 50$ µm yields $|\nabla\vec{B}| \approx 75$ T/m.

This configuration yields a rather high gradient. However, these numbers are only true in the case of large electrode gaps (or DC currents) because high frequency currents induce opposing currents in nearby electrodes. We will now move to more complicated models to describe these fields in a more realistic way.

2.2.2 More complex models

Our simulations (using the method of finite elements – FEM) for multi-layer structures have consistently shown that $h \approx 2d$. Therefore we conclude that the three current model to describe the current layout is incomplete. This was also suggest by Wahnschaffe *et al.* [17]. They used an analytic model which points to the importance of including induced currents in the nearby electrodes. In their work, a single-surface technology with thick electrodes (5 µm) placed far from a ground plane was studied. In this case, the coupling between neighbouring electrodes played an important role which resulted in a low magnetic field minimum position. Because of this, overlapping the magnetic field minimum and the pseudopotential tube could not be realized with the three MW lines placed between the RF electrodes. Therefore, an asymmetric five-wire SET had to be used. As the current amplitudes induced in the neighbouring electrodes are difficult to estimate not much new information is gained from those

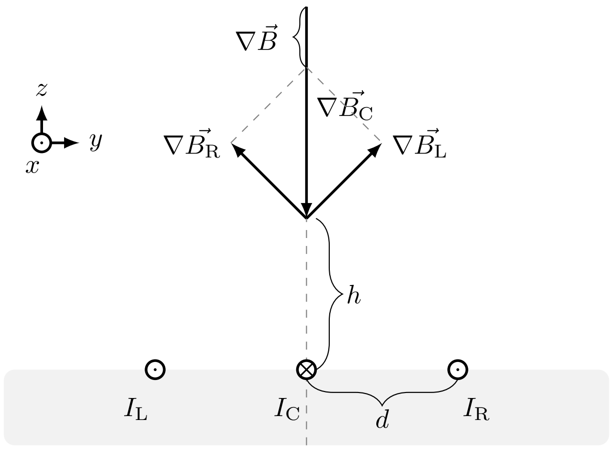

Figure 2.3: Adding magnetic field gradients from the three individual wires produces a net gradient which does not cancel out at the B-field null.

models. In our case the induced currents in the neighbouring electrodes are weak because they are far compared to the ground plane under the electrodes. I will show in the next section, that in this case a more suitable model takes into account the currents induced in the ground plane beneath the electrodes rather the ones in neighbouring electrodes. In this case, the magnetic field minimum position will be higher, which allows to use a symmetric design.

2.2.3 Three wires above a grounded plane

One of the design goals is to find an electrode configuration which overlaps the B-field minimum and the pseudopotential tube. The lowest possible pseudopotential tube height for a symmetric 5-wire SET is achieved in the limit of infinitely narrow RF electrodes (see Subsection 4.1.1). Wider RF electrodes provide a larger trap depth and a higher minimum position (Eq. 4.1). The three wire solution ($h = d$) suggests, that at least one of the RF electrodes should be placed between or superposed with one of the MW lines. This would either mean that we can not use a meander-like structure, or we would have to use a non-symmetric configuration. Both of these options significantly increase control complexity and spurious coupling-related problems. We have been considering multi-layer technologies (see Section 4.1) which could allow for placing several conducting metallic ground planes under the current carrying lines. As we have seen, this significantly affects the position of the B-field minimum.

I have used the *image current theory*[F] [35, p. 42] to analyze the effect of a single ground plane under the three-wire-configuration.

Solving this configuration for the B-field minimum gives

$$h_{\min} = \sqrt{\frac{d^2(I_C + I_S) + \sqrt{4d^4 I_C I_S + d^4 I_S^2 + 4d^2x^2 I_C(2I_S - I_C)}}{2I_S - I_C} + x^2} - x \ , \quad (2.12a)$$

$$\text{for} \quad I_C = I_S \quad \rightarrow \quad h_{min} = \sqrt{2d^2 + x^2 + \sqrt{5d^4 + 4d^2x^2}} - x \approx 2d \ , \quad (2.12b)$$

$$\text{for} \quad \xi = \frac{I_C}{I_S} \quad \rightarrow \quad h_{min} \approx d\sqrt{\frac{1 + \xi + \sqrt{1 + 4\xi}}{2 - \xi}} \ . \quad (2.12c)$$

[F] Let us have a surface current density $\vec{J}$ parallel to an infinite metallic ground plane at distance h. The image theory states that this ground plane can be substituted with a surface current density $-\vec{J}$ placed on the opposite side of the plane at distance $2h$ from the original charge [35, p. 42].

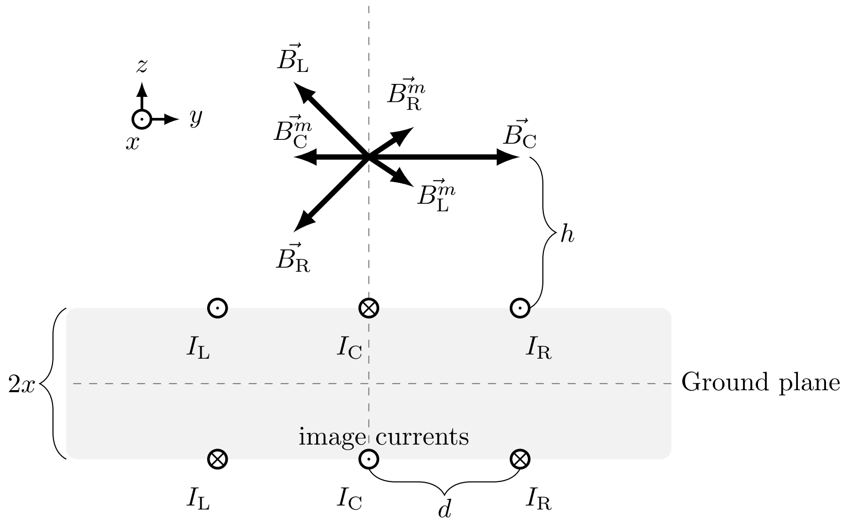

Figure 2.4: The ground plane which is positioned under the electrodes introduces an extra set of induced currents which have to be taken into account. The ground plane can be replaced with *image currents* for an analytic understanding.

This result agrees with our simulation results where $d = 25$ µm, (measured to the center of the side electrode) $x = 1$ µm (center-to-center distance of two metallic layers) and corresponding ion position is $h \approx 50$ µm. It also describes how tuning the current ratio ξ changes the magnetic field minimum position. We get a more accurate model, if we use Eq. 2.7 to take the length of the wires into account but the solution does not have a convenient analytic form.

2.2.4 Realizable geometries for the three-wire configuration

In the following section I will discuss advantages and disadvantages of different planar 3-wire configurations.

Firstly, a simple but experimentally inconvenient design would have three individual wires (see Fig. 2.5 a)) with controlled currents. On one hand this leads to complete control over the system. On the other hand it introduces five independent parameters (three current intensities and two relative phases) [12, 20].

An easy way to reduce complexity is to wrap a single wire into a meander shape line (see Fig. 2.5 b)) [17]. This design suffers from accumulating relative phase between the lines and an asymmetry with respect to the direction of the trap axis as the turnarounds break symmetry. The field from the turnarounds can be shielded at the expense of making a longer meander and therefore increasing the phase difference. For a meander design it is impossible to completely cancel residual fields in the center of the trap due to its asymmetry and the phase mismatch issue. A fixed relative phase means that $I_L < I_C < I_R$ (or vice versa) which means, that the minimum is not positioned exactly above the center of the central wire.

A third option is to use a trident design (see Fig. 2.5 c)) as proposed in this thesis. This design is symmetric along the trap axis. The phase and amplitude of I_L and I_R are equal when there are no relevant fabrication errors. It also opens the possibility of controlling the magnetic-field minimum position by using the two outputs (P1 and P2 on Fig.2.5 c)) of the trident as a current divider tuned with external termination. The trident design has also two disadvantages. Firstly, when the two side-wires are not fabricated to have equal width, then the position of the B-field null will shift off the trap axis (this is also true for the meander). Secondly, the total current inserted to the circuit will divide into two wires, so effectively four times more power is required for a similar gradient value when compared to the meander.

If the trap is three dimensional (the ion can be placed between the electrodes) then only two current carrying conductors are needed to produce a magnetic field minimum with a non-vanishing gradient. These systems are however very sensitive to current/phase differences in the two wires. The analysis of these systems is beyond the scope of this thesis.

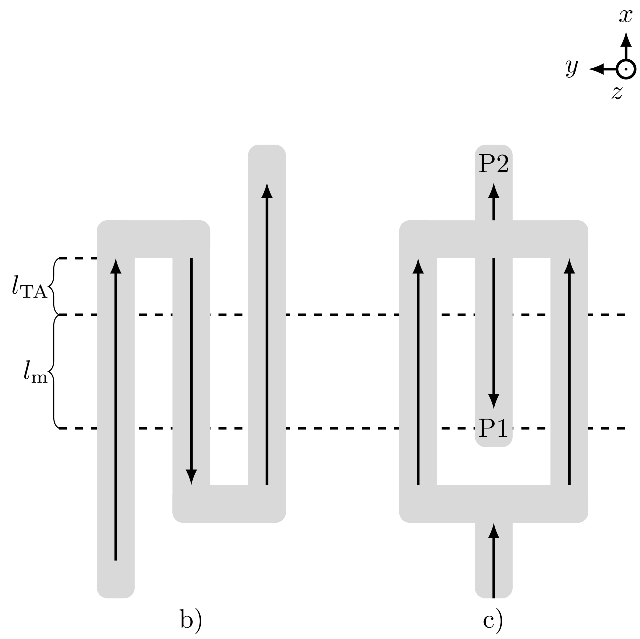

Figure 2.5: Possible three wire geometries. a) Three individually controlled lines b) Meander c) Trident. For the meander and the trident the electrode sections between the dashed lines should be visible to the ion and everything else shielded under a grounded surface. The effective length of the meander is then l_{m} and the length of the *turn-around* is l_{TA}. Positions P1 and P2 indicate the two outputs of the trident which can be used for tuning the position of the B-field minimum.

2.2.5 Various electrode configurations

Figure 2.6 shows the schematic cross-section of currently realized traps. Designs a) and b) use individually controlled microwave lines which makes the design tunable. In design b), open-ended $\lambda/2$ resonators were used to superpose RF/DC voltages and MW currents simultaneously in the same electrodes. Three individual lines have each an open-ended resonator and the ion is trapped above the current anti-node in the center of the resonators. Design c) showed very good properties in simulations [17] but the experimental device could never trap ions. Design d) was constructed as a proof of principle to compare simulation and experimental results. The experimenters noticed that by changing the termination of the MWc electrode they were able to shift the microwave null considerably (several microns) [G]. All designs which have been currently realized suffer from strong coupling between the MW lines to the surrounding electrodes since they use fabrication technologies where the ground plane is much farther (therefore the coupling is weaker) than the nearest electrode. I have considered CMOS-like multi-layer technologies in which case a grounded metallic layer is much closer than the nearest electrode [36]. This produces a weak electrode-electrode coupling and a strong electrode-ground coupling.

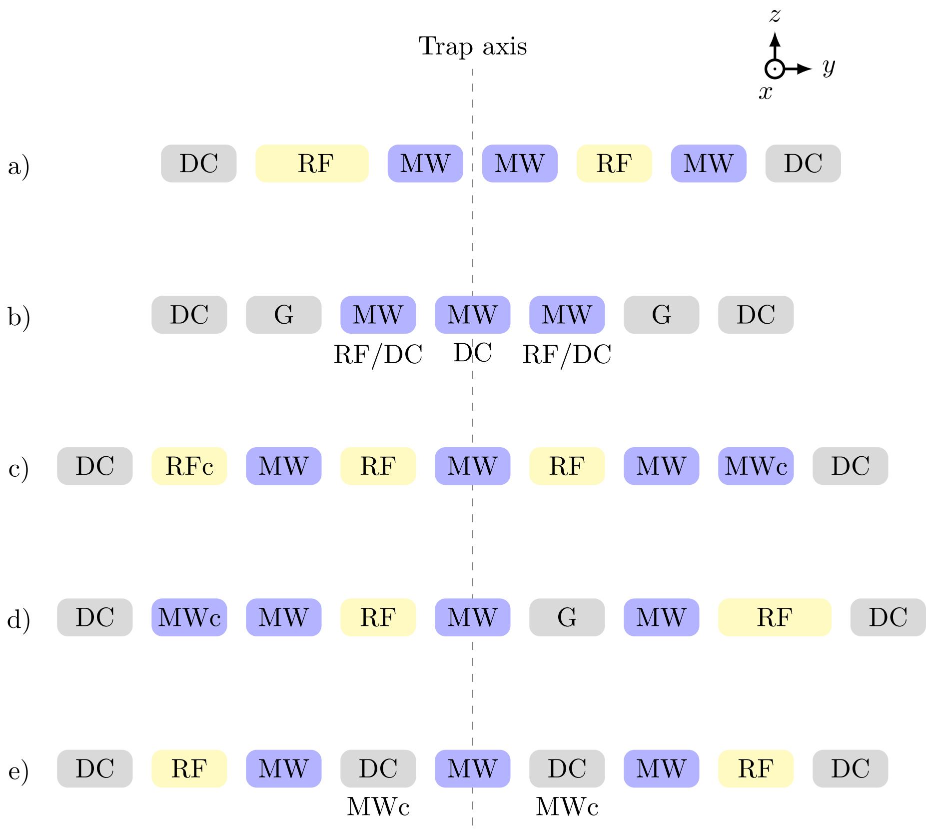

Figure 2.6: Cross sections of various proposed or realized electrode configurations. Notation: MW - microwave; MWc - microwave carrier drive; RF - radiofrequency; DC - slow potentials for ion confinement. a) - NIST [12, 19]; b) Oxford [9, 20, 14]; c) Hannover proposal [17]; d) Hannover experiment [11]; e) Design proposed by this thesis. Note that this design is the only one where the RF electrodes are placed completely outside the MW lines and the DC/MWc is implemented as close to the ion as possible.

[G] Private communication with M. Wahnschaffe.

2.3 Scaling laws for surface traps

I have collected the scaling laws of various important parameters to gain an intuitive understanding of surface electrode traps with integrated microwave structures. I will consider a special case of traps where the thickness t of individual electrodes is fixed[H] but electrode size and separation scales as ρ. I fix the radial motional frequency ω_{r} caused by the pseudopotential confinement. The electrodes are made of superconducting Niobium, which has a critical current density j_{crit}. The MW current is held close to critical current. The goal is to study the scaling of entangling and individual addressing gate times.

Assumptions used:

- $j \propto \rho^0$ – the critical current density j_{crit} in the electrodes is independent of electrode size;
- $\dot{\bar{n}} \propto \frac{S_{\mathrm{E}}(\omega)}{\omega}$ – where $\dot{\bar{n}}$ is the rate of change of the mean thermal occupation number, S_E spectral density of electric field fluctuations and ω is the frequency of the motional mode under consideration (for us the radial mode) [33];
- $S_{\mathrm{E}} \propto h^{-\alpha}\omega^{-\beta}$ – where h is the ion-electrode separation. The mechanism of surface heating is not well understood and a range of values have been offered for α and β. For example in Ref. [31] $\alpha \approx 3.5$ and $\beta \approx 0.8$ to 1.4;
- $\Delta E \propto V^2\omega_{\mathrm{rf}}^{-2}h^{-2}$ – the depth of the RF pseudopotential for the symmetric five-wire SET (Eq. 4.2);
- $\omega_{\mathrm{r}} \propto Vh^{-2}\omega_{\mathrm{rf}}^{-1}$ – radial frequency due to pseudopotential confinement (Eq. 8b). The RF voltage is V and frequency ω_{rf}. If we fix the depth of the pseudopotential then $\omega_{\mathrm{r}} \propto \sqrt{\Delta E}h^{-1}$.;
- $h \propto \rho$ – the trapping height is proportional to electrode dimensions (Eq. 4.1).

The scaling laws relevant to the microwave gates are:

- $I \propto j\rho \propto \rho$ – critical microwave current in the conductors is proportional to the width of the MW line;
- $B \propto \frac{I}{\rho^{1+\gamma}} \propto \rho^{-\gamma}$ – addressing and stray magnetic field amplitude. The factor $\gamma \geq 0$ describes the currents induced in the neighbouring electrodes which make fields more localized[I].
- $B' \propto \frac{\partial B}{\partial \rho} \propto \frac{I}{\rho^{2+\gamma}} \propto \rho^{-1-\gamma}$ – the gradient of the magnetic field;
- $\tau \propto \frac{\sqrt{\omega m}}{B'} \propto \rho^{(1+\gamma)}$ – the entangling gate time (Eq. 1.18). Note, that $\tau \propto \sqrt{\omega_{\mathrm{r}} m} \propto m^0$ which indicates, that entangling gate time is independent of ion mass for a fixed ω_{rf}.;
- $\eta \propto \frac{B'}{\omega B} \propto \rho^{-1}$ – figure of merit (defined in Ref. [17]).

Conclusions and remarks:

- entangling gate times, figure of merit and carrier driving rates improve as we build smaller traps;
- if we keep the trap depth constant then the entangling gate time scales as $\tau \propto \rho^{0.5+\gamma}$.

[H] Standardized multi-layer fabrication technologies have technological limits.

[I] An infinite thin wire with current I produces a magnetic field amplitude $B = I\mu_0/2\pi r$ at distance r from its center. Let there be a ground plane parallel to the wire at distance x. This can be substituted with an wire with current $-I$ at distance $2x$ from the wire. The magnetic field seen at large distances $r \gg x$ from this system is $B = I\mu_0(r^{-1} - (r+2x)^{-1})/2\pi \approx I\mu_0 x/\pi r^2$. In our case the distance x to the ground plane is fixed and therefore this example yields $B \propto r^{-2}$.

Chapter 3

Superconducting Niobium thin films

Fast MW gates rely on strong magnetic fields and gradients (see Section 1.1). In my case, these fields are the MW near-fields created by currents in electrodes and the field magnitude is proportional to the current amplitude. High currents in small trap structures may lead to temperature fluctuations and even trap breakdown. Superconductors are known for their capability to carry very high currents with very low dissipation. Microfabrication technologies allow for small trap structures [37], can be integrated with microelectronics [32] and produced on an industrial platforms [36]. Superconducting Nb has been used to realize an microfabricated ion trap [38] and to provide magnetic shielding [39]. I will give a short introduction of physics related to thin-film Nb conductors.

Superconductivity (SC) was discovered in 1911 by Heike Kammerlingh Onnes while studying mercury. He observed, that at 4.2 K the electric resistance disappeared. The theoretical description was provided by the phenomenological Ginzburg-Landau theory of SC in 1950 followed by the proposal of the complete microscopic theory of SC by Bardeen, Cooper and Schrieffer (BCS theory) in 1957 [40].

Superconducting materials expel external magnetic fields below a certain critical field value – called the Meissner effect. Superconductors can be divided into two main groups according to how they behave in an external magnetic field. In *Type I* superconductors, the SC is abruptly destroyed if the applied magnetic field rises above a critical field H_{C}. In *Type II* superconductors, raising the external field above H_{C1} allows some magnetic flux to penetrate the material forming a vortex state. At the second critical field (H_{C2}) SC is destroyed. Superconducting materials are characterized with a critical temperature T_{C} and a magnetic field penetration depth $\lambda(T)$ – London depth. Niobium, unlike most pure elemental superconductors, is Type II with $H_{\mathrm{C1}} = 1.1 \times 10^5$ A/m (measured at 1.3 GHz and $T = 6$ K), $T_{\mathrm{C}} = 9.2$ K and $\lambda(T = 0) = 70$ nm [41]. The thermal conductivity of Nb at $T = 6$ K is in the range $K = 30-600$ W/mK and depends on its purity [42]. This is roughly in the same range as thermal conductivities for sapphire, SiO_2, silicon or copper at this temperature [9, p. 175].

One of the companies specializing in multi-layer superconducting technology is Hypres Inc. Superconducting multilayer Nb systems are produced by sputtering thin Nb layers on top of Si substrate. A normal metal layer can be added to provide medium-value resistors, shunting Josephson junctions, etc. Silicon dioxide is deposited to provide insulation between the conducting layers. A typical 4-layer Nb foundry process provided by Hypres provides Nb sheets with layer thickness $100-600$ nm with 10% and SiO_2 (thickness $100-500$ nm) tolerance. Thicker layers can be made by request. The fabrication process involves projection photolitography and etching which may lead to shifts of the object's borders relatively to its image on the mask. This shift (due to enlargement/reduction) is ±200 nm or smaller [A]. What is more, below $T \approx 10$ K, the thermal conductivity of these materials increases with temperature which acts as a stabilizing mechanism for temperature fluctuations.

The London depth for a material depends on its purity and temperature

$$\lambda(T) = \frac{\lambda_{\mathrm{L}}(0)}{\sqrt{1 - \left(\frac{T}{T_{\mathrm{C}}}\right)^4}} \tag{3.1}$$

where $\lambda_{\mathrm{L}}(0)$ is the London depth at $T = 0$ K. For example, the London depth for Nb at $T = 8$ K is $\lambda \approx 1.5 \times \lambda_{\mathrm{L}}(0)$. It increases with decreasing film thickness substantially if the film thickness is below a few-hundred nanometers [43]. If the superconducting material is at a non-zero temperature then it can be described by a two-fluid model. In this case the total current (with density J) in the wire can be divided into a normal current (with density $J_{\mathrm{n}} = \sigma_1 E$ obeying the Ohm's law) and a supercurrent (density J_{SC}). Here, E is the electric field parallel to J_{n}. The latter obeys the London equation

$$\frac{\partial J_{\mathrm{SC}}}{\partial t} = \frac{E}{\mu_0 \lambda^2} \; . \tag{3.2}$$

We can combine these two currents and relate them to the electric field by defining a complex conductivity σ_{c}

$$J = \sigma_{\mathrm{c}} E = (\sigma_1 - i\sigma_2)E \; , \tag{3.3}$$

where $\sigma_2 = (\omega\mu_0\lambda^2)^{-1}$. The real part of the complex conductivity describes a loss mechanism in the superconductor. The imaginary part relates to kinetic inductance $L_{\mathrm{k}}(\lambda)$ which describes the kinetic energy of the supercurrent. The resonance frequency ω_{r} of a superconducting waveguide resonator (see Section 4.2) will also be temperature dependent due to the temperature dependent inductance $L(\lambda(T))$. This dependency can be written $\omega_{\mathrm{r}} = \omega(T_0)\sqrt{L(\lambda(T_0))/L(\lambda(T))}$ [44]. The resonator experiences a red-shift as the temperature increases because the increasing penetration depth causes the kinetic inductance to rise. This effect is weaker for thicker conductors [44, Fig. 6]. It is also interesting to note, that current density in superconducting strip transmission line is more uniform in thicker transmission lines and for larger London depths (corresponding to higher temperatures) [44, Fig. 3 and 4].

The losses can be described by the intrinsic surface resistance R_{S} which is defined as $R_{\mathrm{S}} = \omega^2\mu_0^2\sigma_1\lambda^3$. This formula can be used together with Eq. 4.9 to evaluate the attenuation due to conductor loss. For $\omega = 2\pi \times 1.08$ GHz, $T = 6$ K, $W = 10$ µm, $z_0 = 8.46$ Ohm and $\sigma_1 = 10^6$ (Ohm m)$^{-1}$ we get $R_{\mathrm{S}} = 3.3 \times 10^{-14}$ Ohm and attenuation $\alpha = 3.9 \times 10^{-10}$ m^{-1}. The real part of the conductivity is material dependent and should be experimentally measured for the specific sample. The losses increase with rising temperature which in case of a resonator cause the broadening of the resonance peak.

Experiments using superconductors have to be operated in a helium-based cryostat to reach temperatures below T_{C} and have sufficient cooling power. The critical current which breaks the SC is determined by the critical field strength of the superconductor. We can estimate the critical current density by considering an external magnetic field H_{C} applied parallel to an infinite Nb plane in y-direction. Let the half-space $x \geq 0$ pure Nb. The magnetic field inside the Niobium is attenuated exponentially due the Meissner effect

$$H_y(x) = H_{\mathrm{C}} e^{-x/\lambda} \; . \tag{3.4}$$

[A] According to Hypres 4-layer process Design Rules – http://www.hypres.com/foundry/niobium-process/

The supercurrent density flowing in the thin surface layer can be computed from Maxwell's equation

$$\vec{\nabla} \times \vec{H} = \vec{j} \ . \tag{3.5}$$

For this case

$$\frac{\partial H_y}{\partial x} = -\frac{H_y(x)}{\lambda} = j_z(x) \ . \tag{3.6}$$

We can express the current density $j_z(x) = -j_\mathrm{C} e^{-x/\lambda}$ where the critical current density is $j_\mathrm{C} = H_\mathrm{C}/\lambda$. For $H_\mathrm{C1} = 1.1 \times 10^5$ A/m $\rightarrow$ $j_\mathrm{C} = 1.6 \times 10^{12}$ A/m^2. We can estimate the critical current through a strip (along z) with width W, which is much thicker than λ by integrating

$$I_\mathrm{crit} = W \int_0^\infty j_z(x) dx = W H_\mathrm{C} \ . \tag{3.7}$$

The estimated critical current (for the lower critical field) through a strip with $W =$ 10 μm is $I_\mathrm{crit} = 1.1$ A.

Chapter 4

Ion traps for fast entangling microwave gates

This chapter discusses the main results of developing an ion trap optimized for fast high-fidelity entangling gates using MW near-fields. The design of the trap and the simulation methods are presented. The study towards individual ion addressing (IIA) is presented in the following Chapter 5.

The requirements for driving magnetic field driven gates have been listed in Section 2.2. All following designs are based on a multi-layer type architecture which could be realized with superconducting Niobium. It consists of Nb layers (thickness 100-1000 nm) separated by SiO_2 (thickness 100-500 nm)[A]. Superconducting materials are good for carrying high currents and shielding AC fields due to their very high conductivity. The main results of this chapter include the study of advantages gained from implementing a 3D meander design and proof-of-principle results for the trident geometry.

Section 4.1 will introduce our design proposal. This is followed by examples and simulations results of both the 3D meander design (Section 4.1.2) and the trident (Section 4.1.3). Efforts made to maximize the current in the relevant section of the electrode and coupling to a 50 Ohm transmission line are described in Sec. 4.2. Multi-layer systems are advantageous for reducing inter-electrode crosstalk (characterized in Section 4.3) due to many nearby ground planes.

4.1 Design proposal

Here I invetigate flexible designs as shown on Fig. 4.1 and 4.6. They consist of a planar Paul trap (RF electrodes are orange). High-current microwave conductors for driving entangling gates are shown in blue – individually controlled lines, a meander or a trident could be used here. Small current carrying electrodes for IIA are shown in green. These can also be used for axial control (using DC potentials) and compensation of stray electric and magnetic fields. Additional shim electrodes, as indicated on Fig. 4.1 could be added and segmented to allow for micromotion compensation in various zones simultaneously. The goal here is to present a multi-functional design to demonstrate the various possibilities of multi-layer architecture, low inter-electrode crosstalk and good shielding properties. These systems have a clear advantage compared to single-layer systems where hiding sections of the electrodes below ground planes and "island" electrodes are not possible.

[A] Based on Hypres Inc. foundry manuals (http://www.hypres.com/foundry/niobium-process/) and private communication.

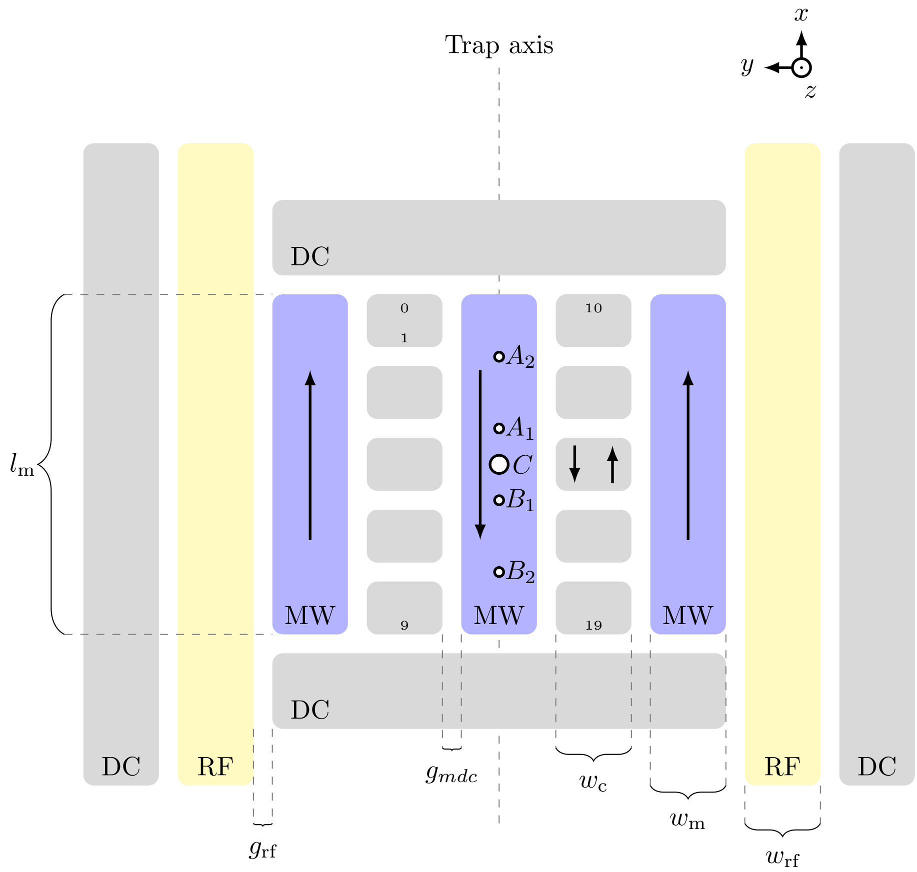

Figure 4.1: Proposed trap layout. The main trapping position is marked with C and possible single-ion-addressing positions with $A_{1,2}, B_{1,2}$. Arrows on the microwave (MW) lines show the current directions during one half of the microwave period. The three MW lines could be individually controlled, sections of a meander or a trident. The small addressing electrodes (one marked with $\downarrow\uparrow$) can be used for both DC control and applying magnetic fields. The numbering (from top to bottom, left to right) indicates the corresponding port number (for following the S-matrix in Fig. 4.13). The large DC electrodes can be used as shim electrodes for compensating micromotion and rotating the pseudopotential eigenaxis.

4.1.1 Simulation results and settings

I used Ansoft software Ansys HFSS (v. 16) to simulate the microwave frequency electromagnetic fields in and near the trap structure. This yields a complex magnetic field value at every mesh point. The meshing is done adaptively and the maximal mesh step is defined. This means that the software automatically meshes regions with rapidly changing field (and geometry) with a higher density. The simulation results were then fitted and analyzed with external software (Python, Mathematica). A fitting model presented in Ref. [11] has been used to fit the magnetic field data around the minimum with a quadrupole field. The complex magnetic field and its gradient at the position of the minimum with their orientation can be extracted.

In order to have standardized results, a layer thickness of 1 μm was used for every Nb layer (simulated as "perfect conductor") and 500 nm[B] for every SiO_2 layer (with relative permittivity $\epsilon = 4$ and dielectric loss tangent 0.005 [45]). Simulating thinner layers led to convergence and run-time problems. The operation temperature of this trap needs to be below the critical temperature ($T_c = 9.2$ K) of Nb in order to remain superconducting. For the substrate of the thin layers 100 μm of Si ($\epsilon = 11.9$ and loss tangent 10^{-4} [46]) on top of 100 μm of copper was simulated. The conductivity of copper was taken $\sigma = 1.5 \times 10^8$ Ohm/cm which corresponds to temperatures from $1 - 20$ K [47]. Both of these layers would be thicker in a real device. However, I found that making these layers thicker in the simulation would prolong the simulation time and give no qualitative insight. During working with these simulations the "multiscale modeling problem[C]" [48] was often encountered.

All the simulations were run at a frequency of 1.08255 GHz[D] with radiative boundary conditions. The surrounding vacuum space around the chip was extended enough to have no measurable effect on the near-field value at the minimum position. The density of mesh-points is highest in the proximity of the trapping position for an accurate result.

Current distribution in the electrodes

Figure 4.2 depicts the surface-current distribution simulated for 3D meander trap design. The surface-current distribution for a trident with $I_S = I_C$ looks nearly identical. From these simulations we conclude that:

- current crowding happens on the sides of the electrodes and especially on the sides closest to ground planes, which means that the waveguide acts effectively as a microstrip;
- strong surface currents are induced around vias, which suggest that these regions may experience the breakdown of superconductivity first;
- the MW fields couple strongly to the ground plane under the electrodes rather than to the neighbouring electrodes. This is a important difference to single-surface systems (all currently realized systems), where the coupling to the neighbouring electrodes was an important effect [10, 19, 17].

[B] These numbers were proposed by Hypres Inc.

[C] Multiscale modeling is the field of solving problems which have important features at multiple scale. In this case the wavelength of the radiation is measured in centimeters, the electrodes and near-field features in micrometers and the relevant scale for the fields inside electrodes is nanometers.

[D] The transition $|F = 2, m_F = 1\rangle \rightarrow |1, 1\rangle$ in Be^+ is first-order magnetic field-independent at 22.3 mT.

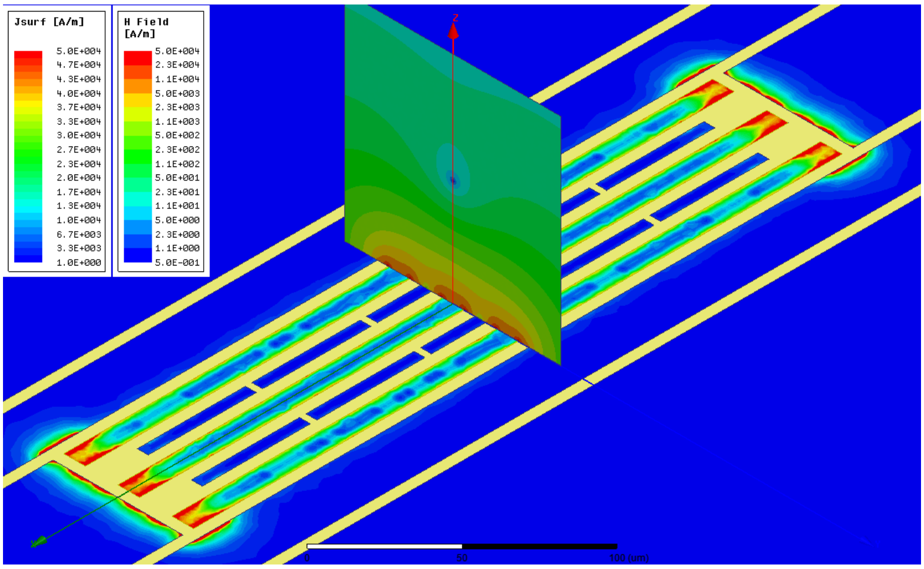

Figure 4.2: Simulation results obtained from Ansys HFSS. The bulk of the microwave current flows on the sides of the meander line. Microwave currents are induced in neighbouring electrodes mainly close to vias. The yellow material in the electrode gaps is SiO_2. The input power was 1 W through a 50 Ohm source.

Radial and axial magnetic fields for magnetic gradient gates

Our goal for magnetic gradient gates is to realize a near-field where the residual field is minimized at the ion trapping location. Due to symmetry, the three long meander segments create mostly a radial field. A residual axial field is generated if the trap geometry is asymmetric with respect to the xz-plane. The meander design violates this symmetry and therefore an extra effort for burying the input/output and turn-around sections has been made. The trident configuration does not violate this symmetry. It is asymmetric with respect to the radial trapping plane but this asymmetry can only produce radial fields which do not contribute to the stray fields but alters slightly the height of the magnetic field minimum.

Studying the near-field distribution on the xz-plane (see Fig. 4.4) reveals the tubular structure of the magnetic field null region. For the meander, this "tube" is parallel to the trap surface in the center of the trap (over a 200 µm long region for $l_m = 250$ µm) and then curves upwards towards the ends of the MW lines. However, for the trident the field minimum tube forms a straight line even close to the ends of the MW lines. This line is slightly lower on the input side of the trident due to the slight asymmetry along the x axis. This could be seen as a useful property – the ions can be moved along the trap axis to find the intersection region of the pseudopotential and magnetic field minimum.

Radio-frequency electric fields

The position of the pseudopotential null is determined by the width of the RF electrodes (w_{rf}) together with the RF-RF electrode distance $D = 3w_m + 2w_c + 4g_{mdc} + 2g_{rf}$ (see Fig. 4.1). We have fixed the RF-DC gap ($g_{rf} = 5$ µm) as is typical for many surface traps. I have chosen to control the position of the pseudopotential only by modifying w_{rf} as the magnetic field configuration depends on it weakly. The height h of the magnetic field minimum for the symmetric five-wire SET can be expressed

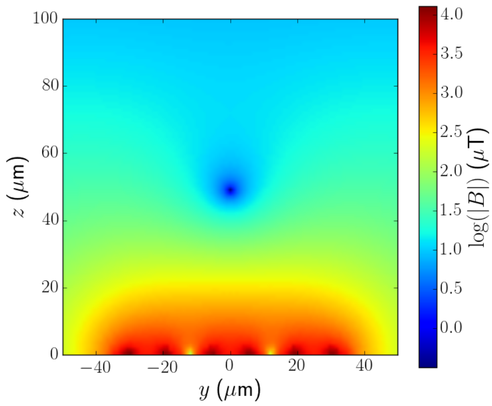

(a)

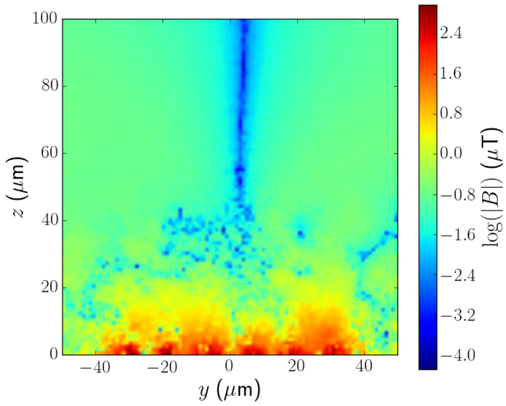

(b)

Figure 4.3: a) Radial and b) axial magnetic field amplitudes in the radial plane of the trap at $x = 0$. These fields describe a trident design with $l_\mathrm{m} = 300$ μm with 1 W input power through a 50 Ohm port. Notice the difference in the scales between a) and b). The axial fields have been compensated below computational noise level. In both cases, the current crowding towards the edges of the electrodes can be seen. The fields in the radial plane of the trap look similar for all three-wire systems.

as [49]

$$h = \frac{d_\mathrm{rf}}{2}\sqrt{1+\frac{2w_\mathrm{rf}}{d_\mathrm{rf}}}\ . \tag{4.1}$$

The trap depth can be written as [50]

$$\Delta E = \frac{e^2 V_\mathrm{rf}^2}{\pi^2 m \omega_\mathrm{rf}^2 h^2}\kappa\ , \tag{4.2}$$

where the geometric factor

$$\kappa = \left[\frac{\sqrt{w^2 D(D+2w)}}{2(w+D)^2\left(1+\frac{\sqrt{D(D+2w)}}{D+w}\right)}\right]^2\ . \tag{4.3}$$

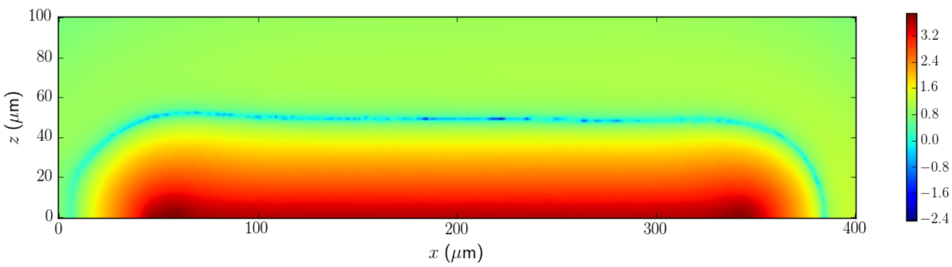

Figure 4.4: Magnitude of the radial magnetic field produced in the xz-plane. The trident ($l_\mathrm{m} = 300$ μm) is positioned at $z = -1\ldots 0$ μm and $x = -150\ldots 150$ μm. Notice, that the minimum is slightly higher on the left side (termination to ground P1). This property can be used to passively minimize stray fields by positioning the ions in the intersection region of the pseudopotential and the magnetic field minimum.

These equations apply for long RF electrodes when no DC potentials are applied. The notation has be shortened for convenience: $w_{\mathrm{rf}} \to w$.

In the current design $D = 70$ µm and the design target for trap height is $h = 50$ µm which gives $w_{\mathrm{rf}} \approx 36$µm. The goal is to achieve low radial frequencies without loosing the ion. I constrain the trap depth to $\Delta E > 10 \times 10^{-3}$ eV (this corresponds to 116 K). This can be achieved by setting $V_{\mathrm{rf}} = 37$ V at $\omega_{\mathrm{rf}} = 2\pi \times 100$ MHz. The corresponding radial frequency for Beryllium is $\omega_{\mathrm{r}} = \frac{1}{\pi}\sqrt{\frac{2}{3}}\frac{eV_{\mathrm{rf}}}{mh^2\omega_{\mathrm{rf}}^2} \approx 2\pi \times 11$ MHz and the stability parameters $q = \frac{2geV_{\mathrm{rf}}}{mh^2\omega_{\mathrm{rf}}^2} \approx 0.28$ and $a = \frac{-4eV}{mh^2\omega_{\mathrm{rf}}^2} \approx -0.04$ (for 1 V DC potential). The geometric factor is $g = 0.353$ for a symmetric five wire trap.

4.1.2 3D meander

The use of a single meandering MW conductor for designed near-fields was proposed in Ref. [17]. The analysis for the structure was done for a single layer (2D) geometry with thick (5 μm) electrodes and in the absence of a nearby groundplane. I have studied the use of multilayer metal-semiconductor-metal-etc. technologies to design more elaborate structures. I have buried the input and termination of the MW waveguide and also the turnaround sections to make the meander field appear as symmetric as possible. The length of the buried turnaround segments l_{TA} (see Fig. 2.5) was optimized to minimize residual field at the center of the trap. The optimal length l_{TA} is dependent on the length of the meander because for a long meander the residual field originating from the turnarounds is weak. The length of the meander was optimized to maximize the figure of merit ($\propto B'/B^{\mathrm{E}}$). The length of the segmented electrodes (see Fig. 4.1) was scaled with l_{m} according to $l_{\mathrm{seg}} = \frac{1}{5}(l_{\mathrm{m}} - l_{\mathrm{TG}})$ to fill the gaps between the meander lines. The total length of the gaps $l_{\mathrm{TG}} = 40$ μm was held constant when the meander length was varied. The number of segmentations did not change the field configuration in the ions position in a significant way.

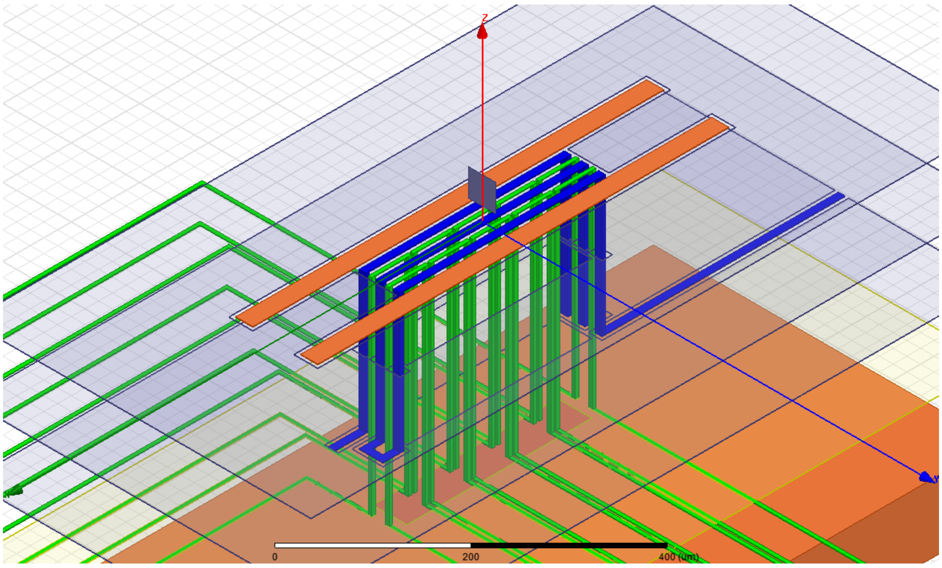

Figure 4.5: A "blown-up" image of the center of the 3D meander trap. The dielectric layers are not visible and expanded hundred fold. Electrodes performing different task have been coloured: orange – RF electrodes (on top) and ground plane (on bottom); blue – meander; green – IIA electrodes; light gray – ground planes; yellow – ground plane dielectric.

[E] The figure of merit describes the ratio of entangling gate drive rate to carrier drive rate (see Section 1.1).

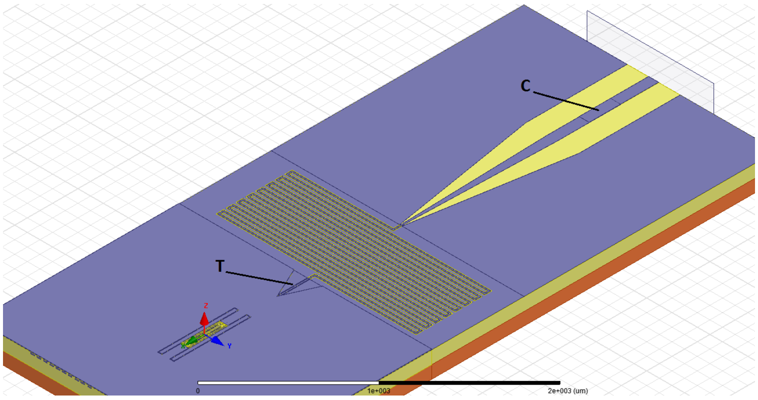

Figure 4.6: The full trap model as simulated for the experiment. The high MW current enters the structure from the right through the transmission line which is capacitatively coupled ("C" marks a plate capacitor) to the quarter-lambda resonator. This chip can be wirebonded to a PCB board which has a tapering to a 50 Ohm waveguide. This is then tapered into the meander to minimize reflections. The on-chip tapering is needed to provide a higher capacitance and more space for wirebonding. The central section holds an extra length of transmission line needed to make up the resonator. The ground plane has been tapered (region "T") for a smooth transition from an uncovered to a covered waveguide. The trapping region (200 μm long) is at the origin of the coordinate axis. The tapered lines for the small segmented electrodes are not shown.

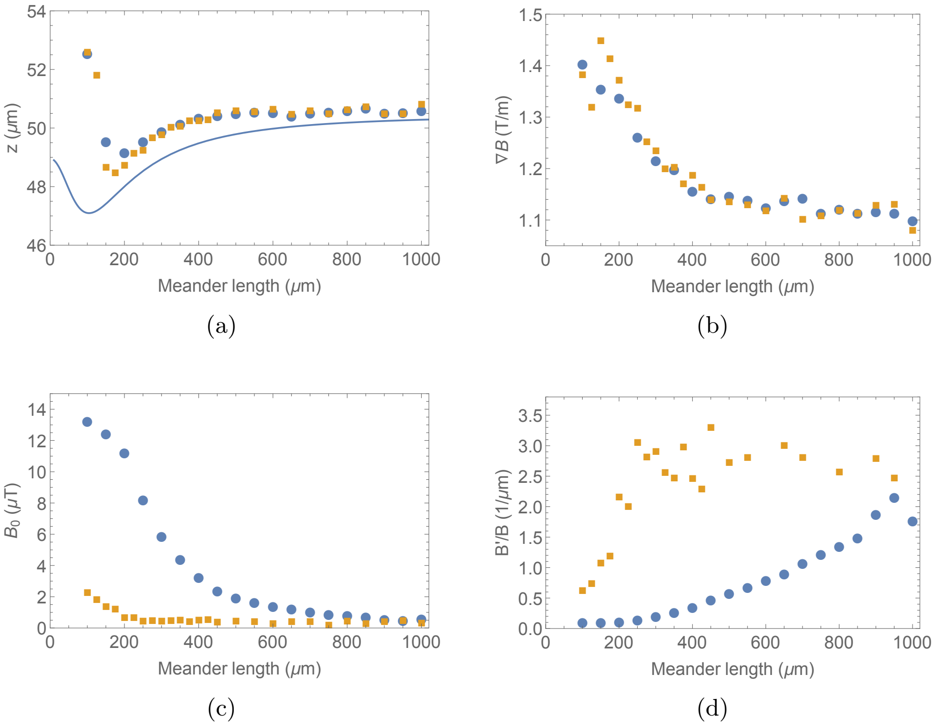

Figure 4.7: Comparison of two meander designs: $l_{\mathrm{TA}} = 0$ μm →(yellow) and $l_{\mathrm{TA}} = 25$ μm →(blue). a) Height of the B-field minimum. b) Magnetic field gradient. c) Residual field magnitude. d) Figure of merit. The length dependence of various parameters for the trident. The input power was $P = 1$ W through a $Z = 50$ Ohm input. The solid line on Fig. 4.7a is the proposed analytic model (see Sec. 2.2.3) extended to take the length of the wires into account (using Eq. 2.7). No free fitting parameters were used. The model is less accurate at small meander lengths because it does not describe the field contributions from the turn-around segments and the effect of vias. The optimal l_{m} range for the case $l_{\mathrm{TA}} = 25$ μm is around $250 - 300$ μm. Around this value we find a compromise between a high gradient and a low residual field. It is possible, that the low field values at longer meander lengths (yellow points at $l_{\mathrm{m}} > 200$ μm) were limited by numeric noise. However, simulations with higher accuracy were beyond the capabilities of the PC used and therefore this remains an open question.

4.1.3 Termination-tuned trident

I introduce and analyze an alternative geometry (see Fig. 4.8 – let us call it a trident because of its resemblance to the weapon of Poseidon) which follows the basic three-wire concept but has several advantages over individually controlled lines and the meander:

- there is no phase difference (due to symmetry) between the left and the right arm, which means that the B-field minimum sits exactly on the symmetry axis of the trident (assuming perfect fabrication);
- if the pseudopotential tube and the B-field null do not overlap perfectly by design then they can be tuned to meet by changing the termination of the trident.

The drawback of the trident design is that the current is divided by the two arms, thus the input current has to be twice as high to realize a field configuration which is comparable to the meander.

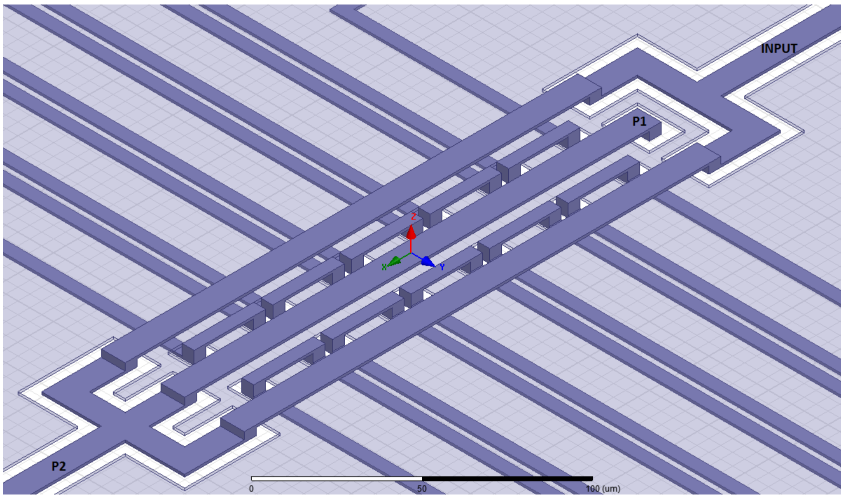

Figure 4.8: The trident, IIA electrodes and the third (counting from top) metallic grounded plane. The white bar is 50 µm. The input of the trident is shown on the right. The central conductor has been grounded. The left-hand side output was grounded further away to provide a desired current distribution $I_\mathrm{S}/I_\mathrm{C} \approx 1$ (see text).

Figure 4.9 shows the simulation results of a possible trident design. The current flowing into the middle conductor was controlled by choosing an appropriate stub length (the left-hand side output on Fig. 4.8). We can see (Fig. 4.9a), that the three-currents-on-ground-plane model (see Section 2.2.3) follows the data points well. The figure of merit for this design (Fig. 4.9d) outperforms even the best meander design (Fig. 4.7d). The rise of the residual field (Fig. 4.9c) in case of shorter electrodes (trapping position is closer to via regions) is strongly suppressed by the symmetry (compared to the meander design Fig. 4.7c). The remaining residual field may originate from the vias (it seems to be dropping off with distance). These values are also so small that they may be the result of insufficient simulation accuracy. These simulations were very time consuming (roughly 12 hours of computational time on a modern PC with 8 cores and 32 GB of RAM). More accurate computation could be done on an cluster computer.

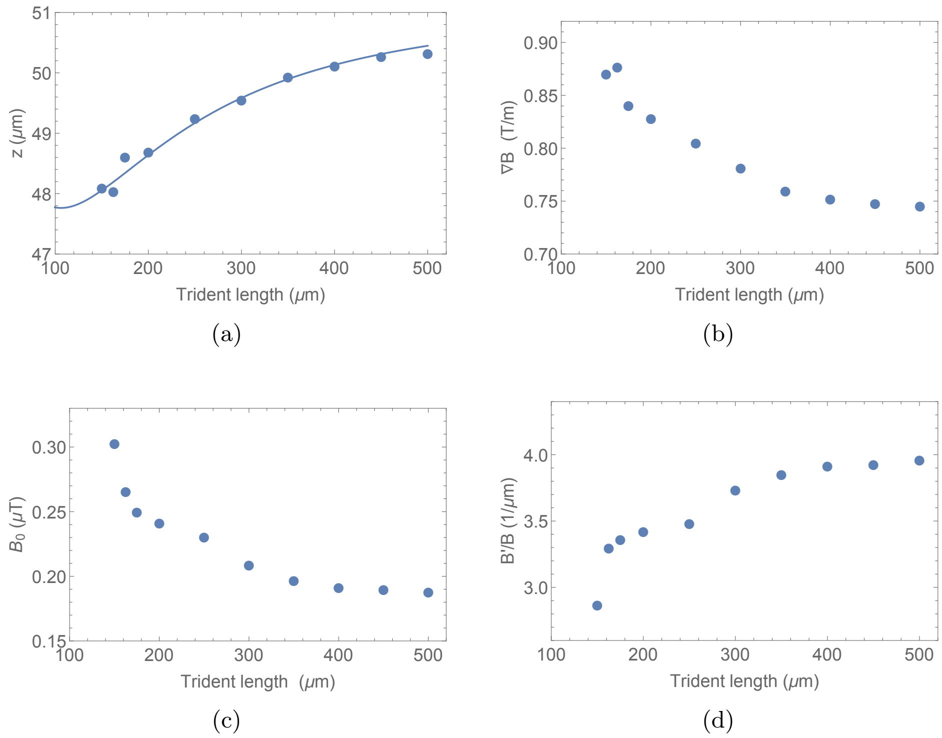

Figure 4.9: a) Height of the B-field minimum. b) Magnetic field gradient. c) Residual field magnitude. d) Figure of merit. The length dependence of various parameters for the trident. A *short-circuited internal stub* with length $1.875 l_{\mathrm{m}}$ (see Fig. 4.1) was used to terminate output P2. The blue line on plot (a) represents the six wire analytic model with $I_{\mathrm{C}}/I_{\mathrm{S}} = 1.018$. The input power was 1 W through a 50 Ohm port.

Tuning termination

By tuning the terminations of the trident outputs, one can control the ratio $I_{\mathrm{C}}/I_{\mathrm{L,R}}$ (see Section 2.2.3). This allows for controlled tuning of the height[F] of the B-field minimum. Our goal is to find a method which is robust to design errors, easy to implement and stable in terms of noise and required control signals. I will list a few possible methods which could be implemented to tune the current ratio in the two trident outputs.

Passive methods

- *Short-circuited internal stub.* Grounding both outputs on the trap chip. Tuning can be achieved by changing the stub length. Can be realized with a sliding conductor (controlled mechanically from outside of the cryo-environment) or by soldering, wirebonding at the right position. Tuning the set-up may take several iterations of cooling, measurement and opening of the trap. Figure 4.10 presents the simulation results of tuning the termination of P2 by varying the length of the conductor l_{P2} before grounding it. The sensitivity to tuning in this case is $\Delta h/\Delta l_{\mathrm{P2}} \approx 25$ nm/μm.
- *Open-ended internal stub.* Both or one (in this case the other output is grounded) output(s) is tapered into a open-ended $\lambda/4$ resonator. The coupling to that resonator can be tuned by sliding a slab of dielectric on top of the resonator.

[F] Due to symmetry the B-field minimum must lie exactly on the symmetry axis of the trident.

- *External stub.* The output(s) is connected to a cable. This cable can be terminated at room temperature with a lumped element. This solution would be convenient to use but long cables are prone to noise pick-up.

Active methods

- *Input an external MW signal.* We consider a situation when the center trident arm (P1 – see Fig. 2.5) is grounded. We input a weak tuning signal I_{t} from the second input (P2). The relative phase and amplitude of I_{t} with respect to the main driving signal determines $I_{\mathrm{C}}/I_{\mathrm{S}}$ and therefore the B-field minimum height. Any relative intensity or phase fluctuation between these two input signals translate into gradient and B-field null position fluctuations[G]. The small segmented IIA electrodes could also be used to shift the B-field minimum. Two of the central IIA electrodes would need to have equal and parallel currents to shift the minimum vertically. However, this is difficult because we need multiple microwave sources with stable amplitudes and phases.

- *On-chip circuit with a varactor diode.* The capacitance of a varactor diode can be tuned with DC voltage. These have been used to build tunable filters [51] and all-CMOS oscillators [52] working in the GHz range. These ideas could be modified to design an active on-chip impedance tuning circuit. Tuning a circuit with DC voltage could be quick, simple and stable.

[G] Let the strong driving signal be $I = I_0 \sin \omega t$ and the tuning signal $I_{\mathrm{t}} = I_{0\mathrm{t}} \sin(\omega t + \varphi)$ ignoring the geometric phase. Then $I_{\mathrm{S}} = \frac{1}{2}(I + (1-c)I_{\mathrm{t}})$ and $I_{\mathrm{C}} = c(I - I_{\mathrm{t}})$ where c determines which fraction of current flows from P2 towards P1.

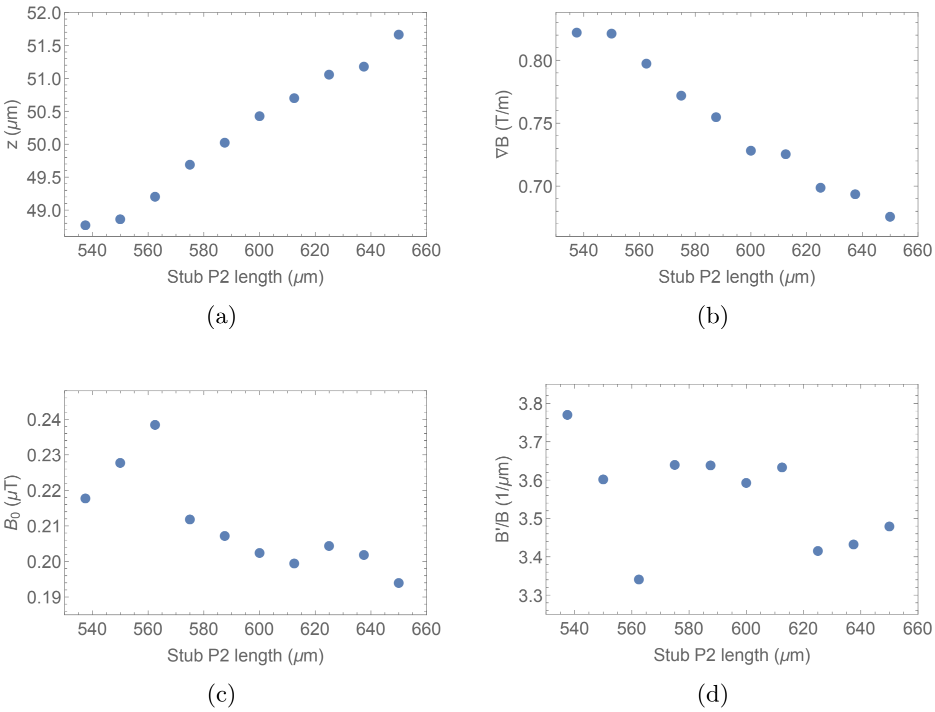

Figure 4.10: Short-circuited internal stub tuning. The port P2 (see Fig. 2.5) was terminated with a short-circuited stub. a) Height of the B-field minimum. b) Magnetic field gradient. c) Residual field magnitude. d) Figure of merit. Tuning the stub length allows to change the height of the magnetic field minimum but it also changes other parameters. The trident length is $l_\mathrm{m} = 300$ μm. The input power is 1 W through a 50 Ohm port.

4.2 Impedance matching

In the following Section, I will introduce the idea of matching the impedance of the MW structure with a short-circuited quarter lambda resonator. This will also provide some power build-up such that less input power is needed to drive the system. I will then present the formulae used to calculated the impedances of various waveguides present in the trap. The tapering from a 50 Ohm cable to the MW structure is discussed in Section 4.2. This Section is finished by presenting the last results and discussing further possibilities (Section 4.2.1).

Transmission lines which connect the microwave signal source with the ion trap chip are typically coaxial cables with 50 Ohm characteristic impedance. This cable is connected to a mounting chip (i.e. an optimized Printable Circuit Board (PCB)) and this chip is wirebonded to the trap chip. The 50 Ohm transmission line can be tapered to impedance-match it to the dimensions of the final conductor. On the trap chip the signal is carried by a conductor-backed-coplanar-waveguide (CBCPWG see Fig. 4.12 a)) through many vias and is finally grounded. Every via, turn in the waveguide and sudden change in waveguide cross-section geometry will lead to back-reflections. High reflections need to be compensated by using a higher input power P_in to realize a desired current in the meander. Grounding the waveguide right after the meander makes sure that the current anti-node is at the grounding position. Because the effective wavelength is much larger than the meander structure it is a good assumption to say that the meander is at the current maximum. A simple resonant system which has a current anti-node at $\lambda_{\mathrm{eff}}/4$ is a short-circuited quarter-lambda resonator. A parallel type of resonance (anti-resonance) can be achieved with this system [35, p. 281].

The voltage reflection at the input port is described by the S_{11}[H] parameter and the power reflection coefficient $R = 1 - T$ is given by its amplitude square $R = |S_{11}|^2$. Here T is the power transmission coefficient and T_{max} is the maximum transmission at resonance $\omega_0 = \omega_{\mathrm{r}}$. We can simulate the S-parameter with Ansys HFSS and fit the extracted data with a Lorentzian curve.

$$R(\omega) = 1 - \frac{T_{\mathrm{max}}}{1 + 4\frac{(\omega-\omega_r)^2}{\Delta^2}} \tag{4.4}$$

where Δ is the full width at half maximum and ω_r the resonance frequency. Figure 4.11 relates the relevant parameters (frequency and transmission) and depicts a possible experimental outcome. The design goal is to achieve a rather low Q cavity. This is useful for two reasons. Firstly, if there is a design fluctuation and $\omega_r \neq \omega_0$ then a rather large fraction of the input power is still transmitted. Secondly, for entangling gates it is necessary to drive a bichromatic signal (red and blue lines on Fig. 4.11) with high currents. Furthermore, the center frequency of the resonator could be slightly higher than ω_0. This is because it is expected that non-linear effects will broaden and red-detune the resonance curve at high driving powers [53] (see also Chapter 3).

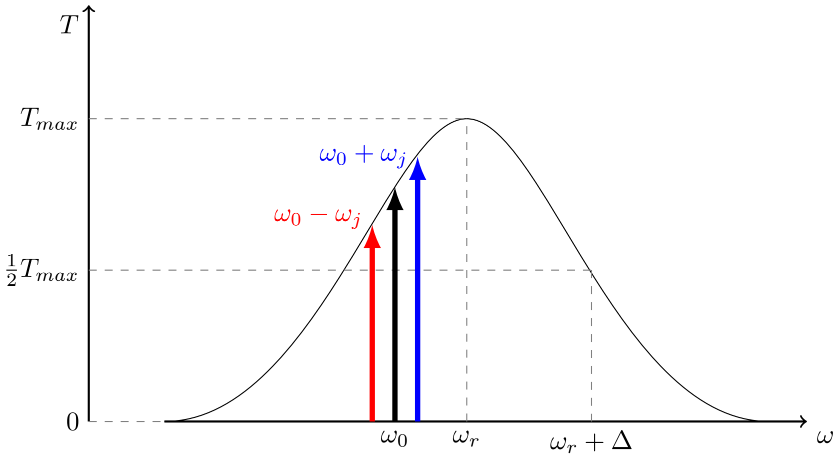

Figure 4.11: The schematic transmission curve of the resonator. The bichromatic signal driven slightly detuned from the red and blue motional sidebands need to have high transmission even if fabrications errors have caused $\omega_r \neq \omega_0$.

Characteristic impedance and loss factor of a coplanar waveguide

I will present the formulae to calculate the characteristic impedance of a conductor-backed-coplanar-waveguide (CBCPWG) and CBCPWG with a grounded coverplane (see Fig. 4.12). The CBCPWG is placed on a dielectric substrate of finite thickness h, dielectric constant ϵ_{r} and loss tangent $\tan\delta$. The effective dielectric constant is

[H] The S_{ii} is the voltage reflection coefficient seen looking into port i when all other ports are terminated in matched loads, and S_{ij} is the transmission coefficient for port j to port i when all other ports are terminated in matched loads [35, p. 179]. An important point to understand about scattering parameters is that the reflection coefficient Γ_{ii} looking into port i is only equal to S_{ii} when all other ports are matched. The scattering parameters are properties of only the network itself and are defined under the condition that all ports are matched [35, p. 183].

given by [54, p. 88]

$$\epsilon_{\rm e} = \frac{1 + \epsilon_r \frac{K(k')K(k_3)}{K(k)K(k_3')}}{1 + \frac{K(k')K(k_3)}{K(k)K(k_3')}} \tag{4.5}$$

and the characteristic line impedance z_0

$$z_0 = \frac{60\pi}{\sqrt{\epsilon_{\rm e}}} \frac{1}{\frac{K(k)}{K(k')} + \frac{K(k_3)}{K(k_3')}} \ , \tag{4.6}$$

where

$$k = a/b \tag{4.7a}$$
$$k_3 = \tanh(\pi a/2h)/\tanh(\pi b/2h) \tag{4.7b}$$
$$k' = \sqrt{1-k^2} \tag{4.7c}$$
$$k_3' = \sqrt{1-k_3^2}\ . \tag{4.7d}$$

Here $K(k)$ represents the complete elliptic integral of the first kind, $a = W/2$ is half the electrode width W and $b = a + g$, where g is the gap width [54, p. 88].

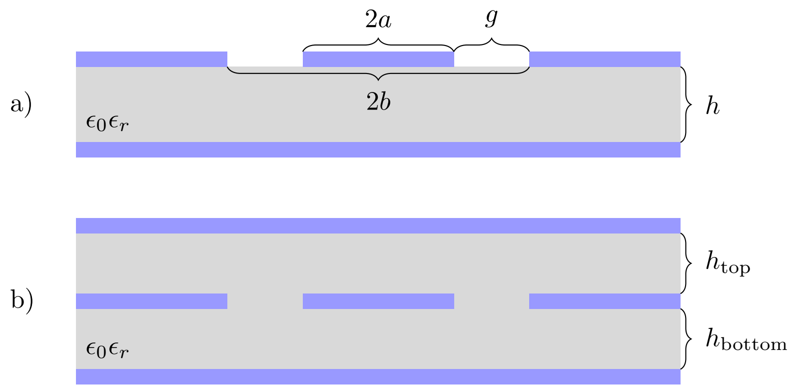

Figure 4.12: Schematics of: a) conductor backed coplanar waveguide (CPCW); b) A CPCW with a cover plane. To reduce the impedance difference between a) and b) the bottom ground plane has been removed such that $h_{\rm bottom} \gg h_{\rm top}$. This reduces the impedance difference between these waveguides because most of the field-lines are between the conductor and the nearest grounded surface. This, in our case, is always the grounded plane (because $h = 0.5$ µm $\ll g = 5$ µm).

In case of the sandwich conductor-backed CPWG (see Fig. 4.12b) the effective dielectric constant is $\epsilon_{\rm e} = \epsilon_{\rm r}$ if $h_{\rm top} = h_{\rm bottom}$. The characteristic impedance is [55]

$$z_{0\rm S} = \frac{30\pi}{\sqrt{\epsilon_{\rm e}}} \frac{1}{\frac{K(k_3)}{K(k_3')}} \ . \tag{4.8}$$

The propagation constant is $\beta = 2\pi f/v_{\rm p}$ and the attenuation due to conductor loss is

$$\alpha_c = \frac{R_{\rm s}}{z_0 W} \ , \tag{4.9}$$

where $R_{\rm s}$ is the surface resistivity. Where $v_{\rm p}$ is the phase speed of the travelling wave and f is the frequency of the signal. The attenuation due to dielectric loss, represented by $\tan\delta$, is

$$\alpha_{\rm d} = \frac{k_0\epsilon_{\rm r}(\epsilon_{\rm r}-1)\tan\delta}{2\sqrt{\epsilon_{\rm e}}(\epsilon_{\rm r}-1)} \ , \tag{4.10}$$

where $k_0 = 2\pi/\lambda$.

The characteristic impedance of a line (see Fig. 4.12a) with $W = 10$ μm, $g = 5$ μm, $h = 0.5$ μm and $\epsilon_\mathrm{r} = 4$ is $z_0 = 8.46$ Ohm. The effective dielectric constant is $\epsilon_\mathrm{e} = 3.79$ and loss factor $\alpha_d = 2.2 \times 10^{-3}$ m^{-1}. The characteristic impedance for the covered line with the same dimensions (see Fig. 4.12b) is $z_{0S} = 4.42$ Ohm. This suggests, that the transition from a covered line to an uncovered lines should be avoided. In our case (the coplanar waveguide acts effectively as a stripline, because $h \ll g$) a simple yet effective solution could be having $h_\mathrm{top} = h_\mathrm{bottom} = 2h$. In this case the covered and uncovered waveguides have roughly equal characteristic impedances. In the current design, I have buried the long subsurface transmission lines in the last metallic layer of the chip. This means, that those lines act effectively as conductor-backed CPWGs with Si replacing vacuum ($h_\mathrm{top} = 0.5$ μm $\ll h_\mathrm{bottom} = 100$ μm). We can use formulae 9 and 10 from Ref. [55] to calculate $\epsilon_\mathrm{effective} = 4.53$ and $z_0 = 7.75$ Ohm. This means, that in our case, the transition from surface to sub-surface waveguide is quite "smooth".

The transition from surface to sub-surface waveguide (from 4.12a to b) in multi-layer electronic structures is realized with vertical inter-layer connectors called vias. In the current design, vias are engineered to continue the waveguide from one layer to the other. In future work (once technological limitations are more clear) a more careful optimization for low reflections and losses could be carried out.

Impedance matching with a tapered line

An important cause for reflections can be non-smooth transitions between waveguides with a large characteristic impedance difference. In our case, the 50 Ohm transmission line needs to be smoothly tapered into the ≈ 8 Ohm MW structure. I have chosen triangular tapering because it is easiest to design and simulate. It also provides a wider impedance-matching region (as a function of taper length) than the exponential taper and has lower peak-point reflection coefficient than the Klopfestein taper. The exponential taper, however, would be preferred if space is a concern, because the zero-reflection exponential taper is twice as short as the corresponding triangular taper [35, p. 261-266].

The reflection amplitude from a triangular taper is

$$|\Gamma| = \frac{1}{2}\log_e\left(\frac{z_\mathrm{load}}{z_0}\right)\left[\frac{\sin(\beta L/2)}{\beta L/2}\right]^2 , \tag{4.11}$$

where L is the length of the taper and $\beta = 2\pi f/v_\mathrm{p}$ is the propagation constant. The impedances z_load and z_0 are the characteristic impedances of the two lines that are being matched.

I would need a $L \approx 70$ mm taper to couple perfectly into the waveguide ($z_0 =$ 8.46 Ohm and $\epsilon_\mathrm{e} = 3.79$) with a 50 Ohm transmission line. If the tapering is made very small compared to this length then $|\Gamma| \approx \frac{1}{2}\log_e\left(\frac{z_\mathrm{load}}{z_0}\right) = 0.88$. This indicates that sufficient space should be reserved for tapering the transmission lines to minimize reflections. I can save valuable space on superconducting chip by tapering the 8 Ohm waveguide only as much as needed for reliable wirebonding and do the bulk of the tapering on the PCB board.

4.2.1 Tuning the resonance frequency

Cryogenic-resonator designs for applications in ion trapping at RF frequencies have been recently studied in Ref. [56] by the Innsbruck group, and the design of optimized superconducting resonant circuits with very high Q values for microwave frequency has been thoroughly studied by the superconducting circuit communities [57]. For the current application however, these existing designs are at either the wrong frequency range or for too low currents.

One possibility to achieve high (≈ 1 A) currents in the MW line while minimizing input losses, is to use a resonant system. In this case, the current in the MW structure would be determined by the circulating power P_c in the resonator, which depends on the quality Q of the resonator and the input power P_in. If the resonator is in equilibrium then $P_\mathrm{c} = QP_\mathrm{in}$.

Our goal is to have a resonant structure at $\omega_0 = 2\pi \times 1.08255$ GHz (see Section 1.3) with a FWHM of $\Delta \approx 2\pi \times 50$ MHz (the quality factor of the effective cavity is therefore $Q = \omega_0/\Delta \approx 20$). We have two independent tunable parameters which we can use to optimize the resonance curve $R(\omega)$. These are the capacitance C (indicated with C on Fig. 4.6) of the incoupling capacitor (which can be tuned by changing the overlap l_o of the capacitor plates) and the resonator length L (the large meandering structure on Fig. 4.6 with length l_r). The resonator has been optimized by minimizing input reflections with the internal gradient decent method using l_o and l_r as parameters. The "rule of thumb" is that the resonance width and frequency depend mainly on C and L correspondingly. Ansys HFSS provides a powerful optimization toolbox for searching for the optimal values. I have been able to reach values of $T_\mathrm{max} \approx 0.3$ for current transmission which means that for 1 W sent to the chip, ≈ 0.84 W is reflected back and the circulating power in the cavity is ≈ 3.2 W. The reflections are very high but the circulating power is still higher than the input. Currently, the main source of reflections could be the sudden transition from an uncovered CBCPWG to a CBCPWG with a groundplane (region "T" on Fig. 4.6). This result could be possibly improved by: optimizing the geometry (optimized tapering; use smooth corners on the waveguides); engineering a controlled loss channel into the system by using on-chip resistors; using software which simulates superconductors more accurately (now they have no losses or kinetic inductance); using a more powerful device (i.e. a cluster computer) to optimize the geometry.

4.3 Inter-electrode crosstalk

We can use the S-matrix to characterize the crosstalk between various electrodes. The goal is to minimize crosstalk between all electrodes to avoid technical problems and achieve a better control. Figure 4.13 shows the amplitude of the S-matrix for the 10 small electrodes, the RF electrode (port 20) and the MW electrode (port 21). The small electrodes have numbered ports from 0 to 19 (as labeled on Fig. 4.1). In the following I will discuss how to interpret this matrix. The short conclusion is that even the strongest unwanted coupling is still only ≈ -45 dB. To put this number into perspective, a coupling of -10 dB between the meander and a nearby electrode in an asymmetric single-surface design was reported in Ref. [11]. This coupling was seen as a limiting feature for the particular design.

The matrix can be seen as consisting of three blocks. The diagonal elements of the matrix (S_{ii}) correspond to the input voltage reflection of port i when all other ports are matched. Every other off-diagonal element ($S_{i,i+1}$ and $S_{i+1,i}$) then corresponds to the transmission coefficient from port i to $i+1$. The main block of the matrix [0:19, 0:19] shows the couplings between the small electrodes. This can be seen as four smaller blocks. Blocks [0:9, 0:9] and [10:19, 10:19] correspond to the inter-electrode coupling along the x-axis. Blocks [0:9, 10:19] and [10:19, 0:9] describe the coupling between the left and right sides. Note that the coupling between the electrodes along the x-axis is dominant over the left-to-right coupling. This is expected, because in the first case transmission lines travel parallel to each other for some considerable length which allows for some capacitative coupling to occur. Nevertheless, these couplings are still weak (≈ -50 dB).

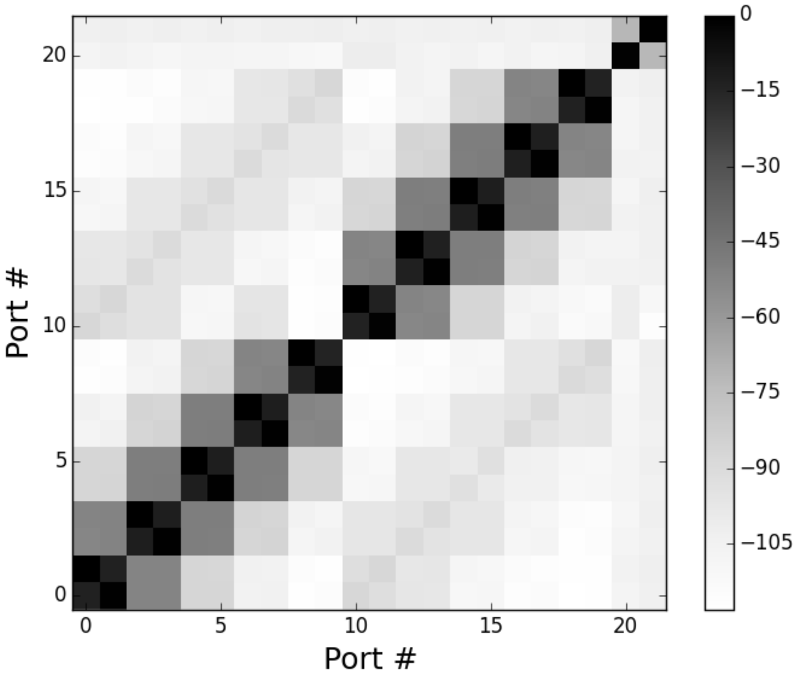

Figure 4.13: The S-matrix of the trap model. The amplitudes of individual matrix elements are shown. The small addressing electrodes are numbered 0-19 (see Fig. 1.2). Ports number 20 and 21 correspond to the inputs of the RF and MW electrodes.

Chapter 5

Individual ion addressing (IIA)

A universal set of quantum gates for an arbitrary number of qubits can be formed by a two-qubit exclusive-OR gate and all one-bit quantum gates [58]. I have presented two designs of an ion trap for fast MW driven multi-qubit entangling gates in Chapter 4. This chapter discusses the possibilities of using MW near-fields for driving single-qubit quantum gates. A good building-block for an universal scalable quantum computer [59] could an be ion-trap chip where all coherent operations are driven by MW near-fields and lasers are only used for readout and cooling.

Addressing individual ions in a linear ion string can be realized using tightly focused laser beams [60] when the beam waist is smaller than the ion-ion separation or using global[A] radiation when the relevant transitions of the irrelevant ions have been detuned by using spatially varying magnetic fields [13, 61]. These methods are technically challenging as laser beams need excellent focusing, beam pointing and stability. Also, producing large magnetic field gradient while still providing good optical access is a non-trivial problem to tackle. I will study a third option, which makes use of MW frequency magnetic near-fields from several small coherent sources to generate high (low) field values at desired locations [10].

In the following I will study a system where two ions are trapped at two zones A and B (see Fig. 4.1) at a fixed height 50 µm. Our goal is to drive a carrier transition on only one of them. Simulation results indicate that the proposed multi-layer design allows for much more localized magnetic fields for single ion addressing than a similar single-surface trap by the Oxford group [10]. In their recent preprint paper they report a Rabi frequency ration (which is equivalent to the magnetic field ratio) of $R_B = 7.2(2) \times 10^{-4}$ between zones separated by ≈ 1 mm using two electrodes, one close to either zone [16]. Our design can reach this level by driving in-phase currents in two addressing zone electrodes if the current amplitudes are roughly matched (meaning they do not differ by more than 15%). What is more, infidelities below 10^{-4} can be achieved by only driving one electrode if the ion-ion separation is ≈ 270 µm (see Fig. 5.2).

In our case, the microwave current carrying electrodes have been hidden below the trap surface and only short sections are exposed on surface (see Fig. 4.1). The magnetic fields produced by the two small electrodes at the outer end of the trap are shown in Fig. 5.1. The symmetry of the design can be exploited to simplify the problem – driving equal currents in neighbouring electrode pairs will create a one-dimensional magnetic field along the trap axis. Zones A, B and C (see Fig. 4.1) mark the ion positions for possible individual addressing. The best position to drive

[A] This can be either at optical or RF frequencies.

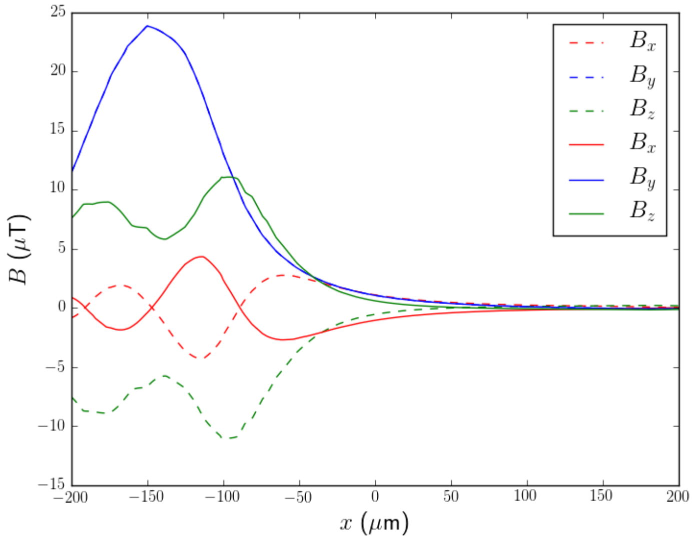

Figure 5.1: Magnetic fields produced by the left-most electrodes. Notice, that B_x and B_y components are anti-symmetric around zero and therefore the total field is one-dimensional when the current amplitudes are equal.

magnetic gradient gates is in the center of the trap (denoted with C). The symmetry of zone C suggests its use for sideband transitions as the field gradient is strongest and the stray field weakest. Zones A and B realize effectively the Aude Craik [10] layout because they each have four electrodes symmetrically around them. Therefore these zones seem potent for high fidelity single ion addressing.

One can follow a simple procedure to simulate the individual addressing of an ion in region A while cancelling the fields at zone B. First the field $\vec{B}_j \propto I_{0j}$ produced by a particular electrode j carrying a current I_{0j} is characterized individually. This can be done by measuring the carrier Rabi rates of a single ion at positions A and B. These rates together with simulation results will give enough information to relate the current I_{0j} through an electrode j to a particular field value at A and B. The relative phases φ_{ij} between electrodes i and j can be calibrated by keeping the currents at a fixed value and scanning the phase for a maximal Rabi rate. The absolute phases are calibrated once all the relative phases are known assuming different electrodes share a MW source. Now, using current amplitudes I_j and phases φ_j we express the total field amplitude in position $\vec{r}$ as

$$\vec{B}(\vec{r}) = \sum_j \vec{B}_j(\vec{r}) \frac{I_j}{I_{0j}} \cos(\varphi_j) \,. \tag{5.1}$$

We then constrain our field configuration for addressing a single ion in zone A and solve to obtain I_j and φ_j

$$\vec{B}(\vec{r_{\mathrm{A}}}) = \vec{B}_{\mathrm{target}} \tag{5.2a}$$
$$\vec{B}(\vec{r_{\mathrm{B}}}) = 0 \,. \tag{5.2b}$$

The target fields define six independent parameters which need control. We have seen that using electrodes pair-wise reduces two field components. This means, that four independent electrodes are required to fully compensate fields in zone B while driving zone A. The gate speed for a fixed ion-ion distance is limited by the maximum current amplitude in the addressing electrodes[B].

5.1 Magnetic fields produced by IIA electrodes

The magnetic fields produced by short IIA electrodes can be used for individual ion addressing for ions in a string (roughly 5 μm separation) if the magnetic field changes considerably over this length. The simplest possible IIA addressing scheme uses only a single electrode (see Fig. 5.2). However, the localization of the magnetic field depends on the electrode size and on the electrode-ion distance. It is possible to fabricate electrodes smaller than the electrode-ion distance. This means, that the electrode acts as a dipole source, with the ion in its far-field. The field dependence on the distance d would be $\propto d^{-2}$ in the absence of induced currents. Because of the induced currents, I can treat the small electrodes rather as a multi-pole field source with a spatial field dependence $d^{-(2+\gamma)}$. In the current design $\gamma \approx 0.49$ (extracted from the linear region of Fig. 5.2). Returning currents in the nearby electrodes cause the magnetic field to completely vanish at a single point if the IIA zone is long enough (see the sharp dips Fig. 5.3). This position could be used to hide a single ion from the magnetic field while driving an ion in other positions.

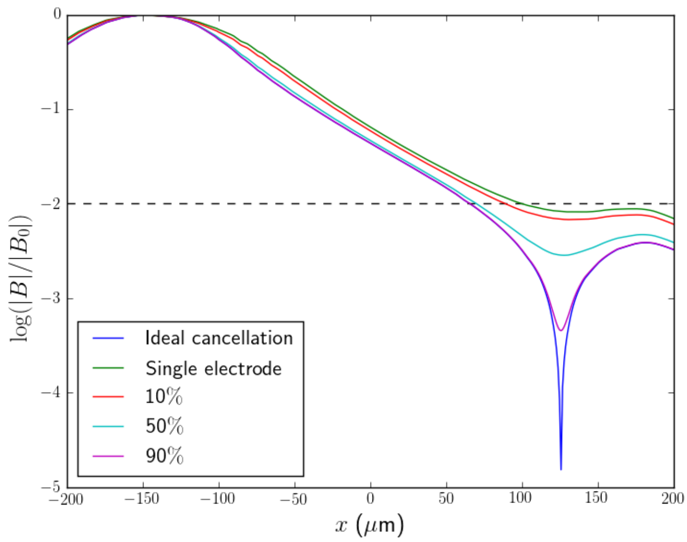

Figure 5.2: Magnetic field magnitude produced along the trap axis at the height of 50 μm by turning on: one electrode (Single electrode); two neighbouring electrodes with equal currents (Perfect cancellation); some fraction of neighbouring electrode current. These electrodes have their center points at $x = -150$ μm and $y = \pm 12.5$ μm (length of the electrode $l_{\text{seg}} = 72$ μm). For the single electrode $B_0 = 180$ μT/A.

As a rough benchmark, we are interested in achieving magnetic field cancellation (conveniently described by the field amplitude ratio $B_\text{A}/B_\text{B} < 10^{-2}$) because this (we will motivate this argument in the next section) is related to infidelities order $< 10^{-4}$.

The simplest solution would be with a single current (I_{left}) carrying electrode producing a well localized field. Figure 5.2 indicates that, at an ion-ion separation of 270 μm, only using a single electrode yields $B_A/B_B < 10^{-2}$ if ion A is positioned at

[B]For the proposed superconducting Nb technology, ≈ 0.5 A of current could be delivered by a 5 μm line.

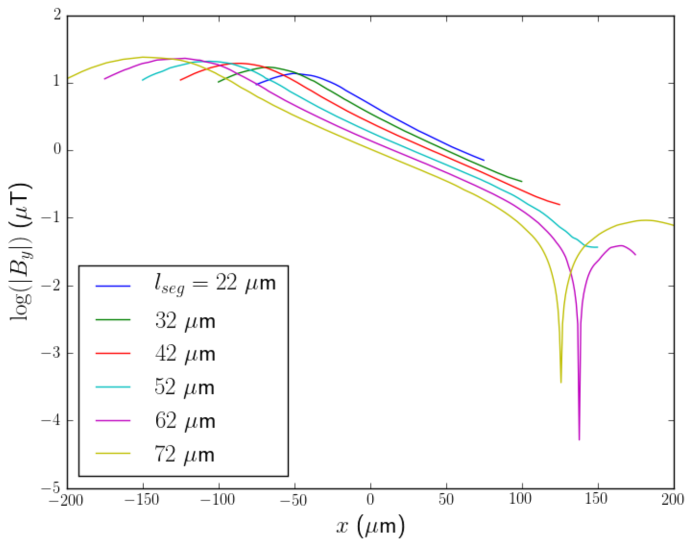

Figure 5.3: Magnetic field y-component magnitude produced along the trap axis at the height of 50 µm by running current (1 W of MW power through a 50 Ohm port) through the left-most small electrode.

the field maximum. Driving the neighbouring electrode will lead to better compensation reaching near-perfect cancellation when $I_{\text{left}} = I_{\text{right}}$ ("Ideal cancellation" on Fig. 5.2).

By controlling the current amplitudes and phases in the IIA electrodes, complicated magnetic field "landscapes" can be created. Figures 5.4 and 5.5 give two examples. We can create four field minima by using five electrode pairs which can be shifted by tuning the relative current intensity between electrodes (see Fig. 5.4). Figure 5.5 describes two pairs of electrodes. Notice the sharp minimum in the field magnitude at -100 % where, in a sub-micron long section, the relative field value is $< 10^{-4}$. We also see, that this region can be shifted in position by tuning the relative current ratio between the two electrode pairs. This could be used to realize "individual ion hiding". Consider an ion string positioned around $x = -70$ µm. All the ions except the one right in the field minimum would be driven with a considerable fraction of the maximum field strength. In case of three ions, two would be addressed and the third hidden from the addressing field. The axial distance between the -1 isolines at -100 % is $\Delta x \approx 5$ µm (see Fig. 5.5). The field magnitude at the bottom of the sharp region (painted light blue on the plot) is zero for an ideal trap. This means, that individual addressing with two ions in the same potential well (ions separated by ≈ 5 µm) could be realized. The fidelity of this operation depends on how well the "hidden" ion can be positioned on the field minimum. The drawback is that the driven ion only experiences $\approx 1/10$ of the peak field.

5.2 IIA fidelity

Let us relate the single ion addressing fidelity to relative magnetic-field values by considering a test scheme with two ions. We start by positioning "target ion" at the location of the maximum magnetic field B_{t}. We then position a "probe ion" at a lower field value B_{p}. Our goal is to drive a single qubit gate in the target ion while leaving the state of the probe ion unchanged. We define the fidelity F of this operation as a projection of the output state $|\varphi\rangle_{\text{out}}$ on the desired ideal output state $|\varphi\rangle_{\text{ideal}} = |\uparrow_{\text{t}}\rangle|\downarrow_{\text{p}}\rangle$. Starting from $|\downarrow_{\text{t}}\rangle|\downarrow_{\text{p}}\rangle$ the states follow the time evolution

$$|\varphi(\tau)\rangle = (\sin(B_{\text{t}}\tau)|\uparrow_{\text{t}}\rangle + \cos(B_{\text{t}}\tau)|\downarrow_{\text{t}}\rangle)(\sin(B_{\text{p}}\tau)|\uparrow_{\text{p}}\rangle + \cos(B_{\text{p}}\tau)|\downarrow_{\text{p}}\rangle) , \tag{5.3}$$

where τ is the effective time. At time $\tau_{\text{g}} = \pi/2B_{\text{t}}$ the target ion is completely in up state. Therefore, the ideal output-state is $|\uparrow_{\text{t}}\rangle|\downarrow_{\text{p}}\rangle$. The fidelity of the operation as define is

$$F = \langle\uparrow_{\text{t}}|\langle\downarrow_{\text{p}}|\varphi(\tau_{\text{g}})\rangle = \cos\left(\frac{\pi B_{\text{p}}}{2B_{\text{t}}}\right) . \tag{5.4}$$

From this equation we conclude that the infidelity related to the field B_{p} is proportional to $(B_{\text{p}}/B_{\text{t}})^2$ if $B_{\text{p}}/B_{\text{t}} \ll 1$. Due to this reason, presenting the magnetic fields normalized and logarithmically makes the plots easier to read.

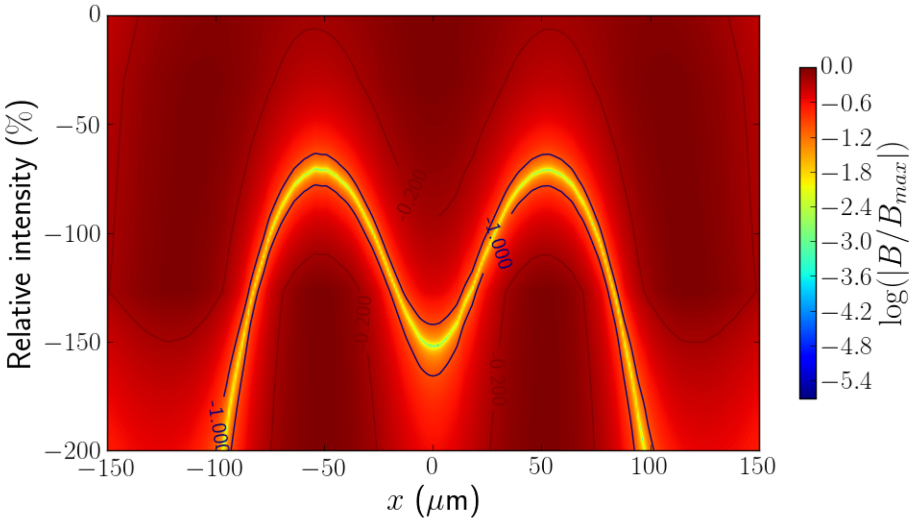

Figure 5.4: Normalized magnetic field y-component (other components are cancelled by symmetry). The currents in the left (small electrodes on the left hand side of the trap axis Fig. 4.1) and right electrode are always pairwise equal and parallel. The current directions in the five small electrodes were oriented according to the following rule $\rightarrow \leftarrow \rightarrow \leftarrow \rightarrow$. The relative intensity is measuring the relative current amplitude of the $\leftarrow$ currents with respect to the $\rightarrow$ currents. Each line (intensity value) has been normalized by its peak value. Here $l_{seg} = 52$ µm.

This mechanism, however, is coherent. This means, that with an appropriate sequence of operations the effect of the remaining field B_{p} can be cancelled.

5.2.1 Gate time

The gate time of a π rotation of the qubit state is (see section 1.1)

$$\tau = \frac{\pi}{\Omega^y} = \frac{2\hbar\pi}{\tilde{B}_y \mu_{y\uparrow\downarrow}} \tag{5.5}$$

where $\tilde{B}_y$ is the amplitude of the magnetic field driving the transition. I will compare three possibilities with increasing number of electrodes (corresponding to increasing complexicity) for individually addressing a single ion. In all of these examples the field magnitude ratio $B_{\text{p}}/B_{\text{t}} < 10^{-2}$.

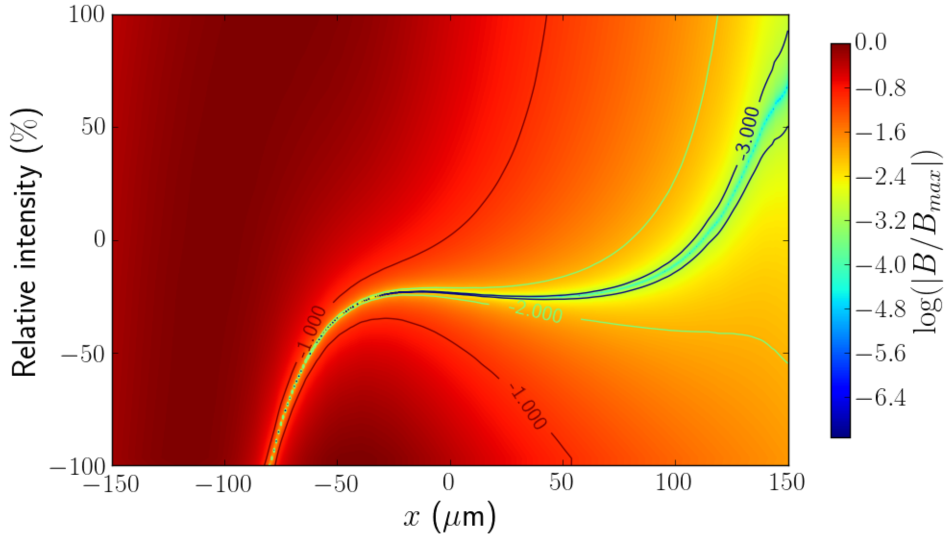

Figure 5.5: Normalized magnetic field y-component produced by electrodes 2B and 1B. The relative intensity indicates the relative current amplitude in electrodes 1B with respect to currents in 2B. At -100 % both electrodes have equal but opposite current and at $+100$ % the currents are equal and parallel. Here $l_{seg} = 52$ µm. The axial distance between the -1 isolines at -100 % is $\Delta x \approx 5$ µm.

- Current is driven through a single electrode (see the green line on Fig. 5.2). The target ion is trapped in a separate potential well. The driven ion is positioned at $x = -150$ µm (above the field maximum) and the probe ion(s) is trapped at $x > 100$ µm. In this configuration the target ion experiences the fastest drive possible with a single electrode. The corresponding π-time is $\tau = 420$ ns/A. The critical current through this electrode is 0.5 A.

- Parallel currents are driven through two neighbouring wires at matching phase and amplitude (see the blue line on Fig. 5.2). Two ions are trapped in the same potential well separated by 5 µm. The probe (hidden) ion is positioned at the field minimum ($x \approx 130$ µm) and the target ion is at $x = 130 \pm 5$ µm. At that position, the driving field is $\approx 10^3$ times smaller than at the field maximum. The corresponding gate time is $\tau \approx 200$ µs/A. Driving close to the critical current would realize a 400 µs π-gate for the target ion.

- Two electrode pairs carry anti-parallel currents (see Fig. 5.5 at -100%). Two ions are trapped in the same potential well separated by 2.5 µm. When the probe ion is positioned at the field minimum, then the field magnitude at the target ion is ≈ 10 times weaker than at the field maximum. This corresponds to a single ion π-time of $\tau \approx 2.1$ µs/A. Driving all the four electrodes close to the critical field would realize a 4.2 µs single qubit gate. Positioning the probe ion is critical because the field minimum is very narrow.

5.3 Alternative uses of IIA electrodes

Although great effort has been made to minimize the stray field for the magnetic gradient gates by design but both technical (fabrication errors) and fundamental (phase difference in the meander lines, remaining asymmetry, etc.) limitations will always produce some finite residual magnetic field. Below are some correction mechanisms which can be applied using the segmented IIA electrodes to improve the magnetic gradient gate.

- Fields produced by the small electrodes can be used to cancel the remaining stray fields generated by the meander. Because the bulk of the magnetic field is cancelled already by design only a small current would be needed to provide the additional correction field.
- The small electrodes could also be used to shift the position of the B-field minimum slightly for a better overlap with the pseudopotential null. For example, say we can realize a large magnetic field gradient of 50 T/m at the B-field minimum by using the meander. This means, that shifting the null position 100 nm would require a 5 μT additional field. This can be achieved by applying roughly 30 mA of of current through one of the central IIA electrodes. This method seems feasible for correcting shifts up to a few hundred nanometers.
- The dynamically decoupled gate (see Subsection 1.2.3) could be implemented by using the segmented addressing electrodes.

Summary and outlook

In this thesis, I have studied multi-layer superconducting ion trap architectures with integrated microwave structures for laserless coherent control of the $^9Be^+$ hyperfine qubit. The main results of the thesis are:

- I have proposed and analyzed a novel symmetric trident geometry for the MW electrode. It produces a higher gradient-to-field ratio and it is tunable which makes it more practical than the monolithic meander-geometry. The optimal trap with a trapping height of 50 μm has: 10 μm wide and 350 μm long trident lines; 5 μm wide and 62 μm long segmented electrodes for individual ion addressing and DC control and 36 μm wide RF rails. All electrodes are separated with 5 μm gaps. The critical current through the individual trident lines is ≈ 1.1 A. This makes it possible to generate a $B' \approx 11$ T/mA field gradient with $B \approx 3$ μT/A residual field. The entangling gate time for two $^9Be^+$ ions driven at 5 MHz rocking mode goes as $\tau = (\tilde{B}'_z \hat{\mu}_{\uparrow\downarrow})^{-1} \times 4.8$ ms. This yields an entangling gate time $\tau \approx 430$ μs/A. Assuming equal currents in all three lines. The probability of off-resonantly flipping one of the qubits during the gate time is 3.2×10^{-7}. The figure of merit $B'/B \approx 4$ (μm)$^{-1}$ corresponds to the effective Lamb-Dicke parameter $\eta \approx 0.04$.
- Extending the meander-geometry to 3D and carefully shielding the turn-around sections showed significant improvement in reducing the residual fields.
- The discussed multi-layer superconducting fabrication technology allows for complicated 3D electrode configurations and provides low inter-electrode cross-talk (< -45 dB). The symmetric design is possible due to the additional ground plane under microwave electrodes which is not possible for single-layer technologies.
- I have studied the use of small segmented electrodes for individual ion addressing. Making use of the trap geometry, very low magnetic fields can be locally achieved. These could be used for high-fidelity sub-microsecond carrier drive of a single ion in a separate potential well and for driving a single ion in a potential well with two ions in few microseconds.

To conclude with, I have designed a novel trap for magnetic field driven QIP. Previously presented ideas about using three MW-lines integrated in a SET [6] for realizing entangling MW gates and using small segmented electrodes [10] for individual ion addressing have been expanded for a multi-layer superconducting design. The main advantages of this design compared to previous work is the low cross-talk and localized fields made available by the multi-layer fabrication technology and the symmetric design.

Outlook

The future outlook of this project is to test the trap. This should begin with testing the capabilities of the fabrication procedure by testing simple components. For example, a few simple waveguide structures could be analyzed by dip-stick measurement to determine the critical currents, voltages and study the break-down effects. In this stage, a varactor-based current divider for the trident should also be designed and tested. A printed circuit board with RF and MW cable connectors with a micromachined slot for the superconducting chip could serve as a convenient base (this could be designed by a company called Rosenberger). The final trap design should be simulated with the exact parameters provided by the chip fabricator. I currently know of two institutions which could provide such fabrication: Lincoln Labs and Hypres Inc. It would be interesting to know how many electrodes can we still reliably control because this determines the complexity of the field "landscape" we can realize for single ion addressing. Achieving high-fidelity individual ion addressing with ions in the same potential well with magnetic near-fields could be shown with this design. Demonstrating an entangling gate with a mono-electrode structure would be the first of this types of experiments.

Appendices

The ponderomotive force

In the pseudopotential approximation, an ions' motion in the RF field can be viewed as a quasi harmonic motion caused by a ponderomotive force

$$\vec{F}_{\mathrm{pm}}(\vec{r}) = -\frac{e}{4m\omega_{\mathrm{rf}}^2}\nabla\vec{E}_{\mathrm{rf}}^2(\vec{r},0)\ , \tag{6}$$

where the inhomogeneous electric driving field $\vec{E_{\mathrm{rf}}} = -\nabla\Phi_{\mathrm{rf}}$ is created by the oscillating RF potentials [29].

We can use a simple harmonic form of to approximate the radially confining potential experienced by the ion $\Phi_{\mathrm{harm}} = \frac{1}{2}vr^2 = \frac{1}{2}m\omega_{\mathrm{r}}^2r^2$. The harmonic potential suggests that the restoring force is linear $\vec{F}_{\mathrm{pm}}(\vec{r}) = \omega_{\mathrm{r}}^2m\vec{r}$ for small deviations $\vec{r}$ from the equilibrium position. The corresponding time-independent potential is called the *pseudopotential* [29]

$$\Phi_{\mathrm{pm}}(\vec{r}) = \frac{e}{4m\omega_{\mathrm{rf}}^2}\vec{E}_{\mathrm{rf}}^2(\vec{r},0)\ . \tag{7}$$

As this potential determines the axial frequency ω_{r}, which is important for the entangling gate, we also note here the scaling with respect trap size scale ρ. We assume, that the RF voltage V will not be limiting us and therefore we can consider it as a parameter.

$$\vec{E}_{\mathrm{rf}} \propto \frac{V}{\rho} \propto \rho^{-1}\ , \tag{8a}$$

$$\vec{F}_{\mathrm{pm}}(\vec{r}) \propto \frac{V^2}{m\omega_{\mathrm{rf}}^2\rho^4}\ \rightarrow\ \omega_{\mathrm{r}} \propto \frac{1}{m\omega_{\mathrm{rf}}\rho^2}\ . \tag{8b}$$

We see that using smaller trap structures, lighter ions and and lower RF frequencies lead to higher radial frequencies. This can be used to calculate the effective radial frequency (trap curvature) from the instantaneous electric potential.

Acknowledgement

Firstly, I would like to thank my supervisor Dr. Joseba Alonso who has been ever helpful on the curvy road of this thesis and pulled me out from the fog of confusion more than once. This project was proposed by Prof. Jonathan Home – I could have not wished for a more exciting, challenging and motivating topic. Secondly, I am grateful for everyone who contributed with valuable discussions: Dr. Martina Wahnschaffe, who helped me with getting the first simulations running and provided valuable information about her experience with microwaves; Prof. Andreas Wallraff and Dr. Anton Potocnik, who shared their experience with superconducting resonators. The wonderful working atmosphere is a common property of the TIQI group.

My life and studies during the past two years in Zurich have been funded by Skype, the Information Technology Foundation for Education and the Estonian Students Fund in USA.

I am forever grateful to my family.

Bibliography

[1] Richard P Feynman. Simulating physics with computers. *International journal of theoretical physics*, 21(6):467–488, 1982.

[2] Jörg Wrachtrup and Fedor Jelezko. Processing quantum information in diamond. *Journal of Physics: Condensed Matter*, 18(21):S807, 2006.

[3] Michel H Devoret and Robert J Schoelkopf. Superconducting circuits for quantum information: an outlook. *Science*, 339(6124):1169–1174, 2013.

[4] Thomas Jennewein, Christoph Simon, Gregor Weihs, Harald Weinfurter, and Anton Zeilinger. Quantum cryptography with entangled photons. *Physical Review Letters*, 84(20):4729, 2000.

[5] C Langer, R Ozeri, John D Jost, J Chiaverini, B DeMarco, A Ben-Kish, RB Blakestad, J Britton, DB Hume, WM Itano, et al. Long-lived qubit memory using atomic ions. *Physical review letters*, 95(6):060502, 2005.

[6] Christian Ospelkaus, Christopher E Langer, Jason M Amini, Kenton R Brown, Dietrich Leibfried, and David J Wineland. Trapped-ion quantum logic gates based on oscillating magnetic fields. *Physical review letters*, 101(9):090502, 2008.

[7] C Ospelkaus, U Warring, Y Colombe, KR Brown, JM Amini, D Leibfried, and DJ Wineland. Microwave quantum logic gates for trapped ions. *Nature*, 476(7359):181–184, 2011.

[8] S. Debnath, N. M. Linke, C. Figgatt, K. A. Landsman, K. Wright, and C. Monroe. Demonstration of a small programmable quantum computer with atomic qubits. *Nature*, 536(7614):63–66, Aug 2016. Letter.

[9] David Thomas Charles Allcock. *Surface-electrode ion traps for scalable quantum computing*. PhD thesis, University of Oxford, 2011.

[10] DPL Aude Craik, NM Linke, TP Harty, CJ Ballance, DM Lucas, AM Steane, and DTC Allcock. Microwave control electrodes for scalable, parallel, single-qubit operations in a surface-electrode ion trap. *Applied Physics B*, 114(1-2):3–10, 2014.

[11] M Wahnschaffe, H Hahn, G Zarantonello, T Dubielzig, S Grondkowski, A Bautista-Salvador, M Kohnen, and C Ospelkaus. Exploring and understanding 2d microwave near-fields using a single ion. *arXiv preprint arXiv:1601.06460*, 2016.

[12] C Ospelkaus, U Warring, Y Colombe, KR Brown, JM Amini, D Leibfried, and DJ Wineland. Microwave quantum logic gates for trapped ions. *Nature*, 476(7359):181–184, 2011.

[13] U Warring, C Ospelkaus, Yves Colombe, R Jördens, D Leibfried, and David J Wineland. Individual-ion addressing with microwave field gradients. *Physical review letters*, 110(17):173002, 2013.

[14] TP Harty, DTC Allcock, CJ Ballance, L Guidoni, HA Janacek, NM Linke, DN Stacey, and DM Lucas. High-fidelity preparation, gates, memory, and readout of a trapped-ion quantum bit. *Physical review letters*, 113(22):220501, 2014.

[15] TP Harty, MA Sepiol, DTC Allcock, CJ Ballance, JE Tarlton, and DM Lucas. High-fidelity trapped-ion quantum logic using near-field microwaves. *arXiv preprint arXiv:1606.08409*, 2016.

[16] D. P. L. Aude Craik, N. M. Linke, M. A. Sepiol, T. P. Harty, C. J. Ballance, D. N. Stacey, A. M. Steane, D. M. Lucas, and D. T. C. Allcock. High-fidelity spatial addressing of ca-43 qubits using near-field microwave control. 2016.

[17] M Carsjens, M Kohnen, T Dubielzig, and C Ospelkaus. Surface-electrode paul trap with optimized near-field microwave control. *Applied Physics B*, 114(1-2):243–250, 2014.

[18] Florian Mintert and Christof Wunderlich. Ion-trap quantum logic using long-wavelength radiation. *Physical Review Letters*, 87(25):257904, 2001.

[19] U Warring, C Ospelkaus, Y Colombe, KR Brown, JM Amini, M Carsjens, D Leibfried, and DJ Wineland. Techniques for microwave near-field quantum control of trapped ions. *Physical Review A*, 87(1):013437, 2013.

[20] DTC Allcock, TP Harty, CJ Ballance, BC Keitch, NM Linke, DN Stacey, and DM Lucas. A microfabricated ion trap with integrated microwave circuitry. *Applied Physics Letters*, 102(4):044103, 2013.

[21] Anders Sørensen and Klaus Mølmer. Quantum computation with ions in thermal motion. *Physical review letters*, 82(9):1971, 1999.

[22] Anders Sørensen and Klaus Mølmer. Entanglement and quantum computation with ions in thermal motion. *Physical Review A*, 62(2):022311, 2000.

[23] GJ Milburn, S Schneider, and DFV James. Ion trap quantum computing with warm ions. *Fortschritte der Physik*, 48(9-11):801–810, 2000.

[24] Hsiang-Yu Lo. *Creation of Squeezed Schrödinger's Cat States in a Mixed-Species Ion Trap*. PhD thesis, Dissertation, ETH-Zürich, 2015, Nr. 22902, 2015.

[25] Mark Fox. *Quantum optics: an introduction*, volume 15. OUP Oxford, 2006.

[26] Wolfgang Paul. Electromagnetic traps for charged and neutral particles. *Reviews of modern physics*, 62(3):531, 1990.

[27] John Chiaverini, R Brad Blakestad, Joe Britton, John D Jost, Chris Langer, Dietrich Leibfried, Roee Ozeri, and David J Wineland. Surface-electrode architecture for ion-trap quantum information processing. *arXiv preprint quant-ph/0501147*, 2005.

[28] Signe Seidelin, John Chiaverini, Rainer Reichle, JJ Bollinger, Didi Leibfried, Joe Britton, JH Wesenberg, RB Blakestad, RJ Epstein, DB Hume, et al. Microfabricated surface-electrode ion trap for scalable quantum information processing. *Physical review letters*, 96(25):253003, 2006.

[29] Florian Michael Leupold. *Bang-bang Control of a Trapped-Ion Oscillator*. PhD thesis, Dissertation, ETH-Zürich, 2015, Nr. 22892, 2015.

[30] Andrew Steane. The ion trap quantum information processor. *Applied Physics B: Lasers and Optics*, 64(6):623–643, 1997.

[31] JM Amini, J Britton, D Leibfried, and David J Wineland. Microfabricated chip traps for ions. *arXiv preprint arXiv:0812.3907*, 2008.

[32] Jungsang Kim, S Pau, Z Ma, HR McLellan, JV Gates, A Kornblit, Richard E Slusher, Robert M Jopson, I Kang, and M Dinu. System design for large-scale ion trap quantum information processor. *Quantum Information & Computation*, 5(7):515–537, 2005.

[33] QA Turchette, BE King, D Leibfried, DM Meekhof, CJ Myatt, MA Rowe, CA Sackett, CS Wood, WM Itano, C Monroe, et al. Heating of trapped ions from the quantum ground state. *Physical Review A*, 61(6):063418, 2000.

[34] Shannon X Wang, Jaroslaw Labaziewicz, Yufei Ge, Ruth Shewmon, and Isaac L Chuang. Individual addressing of ions using magnetic field gradients in a surface-electrode ion trap. *Applied Physics Letters*, 94(9):094103, 2009.

[35] David M Pozar. *Microwave engineering*. John Wiley & Sons, 2009.

[36] Chi Zhang. CMOS fabrication for scalable trapped-ion quantum information processing. Master's thesis, ETH Zurich, Switzerland, 2015.

[37] Marcus D Hughes, Bjoern Lekitsch, Jiddu A Broersma, and Winfried K Hensinger. Microfabricated ion traps. *Contemporary Physics*, 52(6):505–529, 2011.

[38] Shannon X Wang, Yufei Ge, Jaroslaw Labaziewicz, Eric Dauler, Karl Berggren, and Isaac L Chuang. Superconducting microfabricated ion traps. *Applied Physics Letters*, 97(24):244102, 2010.

[39] Shannon X. Wang, Jaroslaw Labaziewicz, Yufei Ge, Ruth Shewmon, and Isaac L. Chuang. Demonstration of a quantum logic gate in a cryogenic surface-electrode ion trap. *Phys. Rev. A*, 81:062332, Jun 2010.

[40] John Bardeen, Leon N Cooper, and John Robert Schrieffer. Theory of superconductivity. *Physical Review*, 108(5):1175, 1957.

[41] Thomas Hays and Hasan Padamsee. Measuring the rf critical field of pb, nb, and nb3sn. *Particle Accelerators*, 61(1):183–192, 1998.

[42] F Koechlin and B Bonin. Parametrization of the niobium thermal conductivity in the superconducting state. *Superconductor Science and Technology*, 9(6):453, 1996.

[43] AI Gubin, KS Ilin, SA Vitusevich, M Siegel, and N Klein. Dependence of magnetic penetration depth on the thickness of superconducting nb thin films. *Physical Review B*, 72(6):064503, 2005.

[44] David M Sheen, Sami M Ali, Daniel E Oates, Richard S Withers, and JA Kong. Current distribution, resistance, and inductance for superconducting strip transmission lines. *IEEE Transactions on Applied Superconductivity*, 1(2):108–115, 1991.

[45] Dale Li, J Gao, JE Austermann, JA Beall, D Becker, H-M Cho, AE Fox, N Halverson, J Henning, GC Hilton, et al. Improvements in silicon oxide dielectric loss for superconducting microwave detector circuits. *IEEE Transactions on Applied Superconductivity*, 23(3):1501204–1501204, 2013.

[46] Jerzy Krupka, Jonathan Breeze, Anthony Centeno, Neil Alford, Thomas Claussen, and Leif Jensen. Measurements of permittivity, dielectric loss tangent, and resistivity of float-zone silicon at microwave frequencies. *IEEE transactions on microwave theory and techniques*, 54(11):3995–4001, 2006.

[47] R Berman and DKC MacDonald. The thermal and electrical conductivity of copper at low temperatures. In *Proceedings of the Royal Society of London A: Mathematical, Physical and Engineering Sciences*, volume 211, pages 122–128. The Royal Society, 1952.

[48] E Weinan and Bjorn Engquist. Multiscale modeling and computation. *Notices of the AMS*, 50(9):1062–1070, 2003.

[49] MG House. Analytic model for electrostatic fields in surface-electrode ion traps. *Physical Review A*, 78(3):033402, 2008.

[50] Altaf H Nizamani and Winfried K Hensinger. Optimum electrode configurations for fast ion separation in microfabricated surface ion traps. *Applied Physics B*, 106(2):327–338, 2012.

[51] Andrew R Brown and Gabriel M Rebeiz. A varactor-tuned rf filter. *IEEE Transactions on Microwave Theory and Techniques*, 48(7):1157–1160, 2000.

[52] Marc Tiebout. A cmos fully integrated 1 ghz and 2 ghz dual band vco with a voltage controlled inductor. pages 799–802, 2002.

[53] MA Golosovsky, HJ Snortland, and MR Beasley. Nonlinear microwave properties of superconducting nb microstrip resonators. *Physical Review B*, 51(10):6462, 1995.

[54] Rainee N Simons. *Coplanar waveguide circuits, components, and systems*, volume 165. John Wiley & Sons, 2004.

[55] Giovanni Ghione and Carlo U Naldi. Coplanar waveguides for mmic applications: Effect of upper shielding, conductor backing, finite-extent ground planes, and line-to-line coupling. *IEEE Transactions on Microwave Theory and Techniques*, 35(3):260–267, 1987.

[56] Matthias F Brandl, Philipp Schindler, Thomas Monz, and Rainer Blatt. Cryogenic resonator design for trapped ion experiments in paul traps. *Applied Physics B*, 122(6):1–9, 2016.

[57] A Megrant, C Neill, R Barends, B Chiaro, Yu Chen, L Feigl, J Kelly, Erik Lucero, Matteo Mariantoni, PJJ OMalley, et al. Planar superconducting resonators with internal quality factors above one million. *Applied Physics Letters*, 100(11):113510, 2012.

[58] Adriano Barenco, Charles H Bennett, Richard Cleve, David P DiVincenzo, Norman Margolus, Peter Shor, Tycho Sleator, John A Smolin, and Harald Weinfurter. Elementary gates for quantum computation. *Physical review A*, 52(5):3457, 1995.

[59] David Kielpinski, Chris Monroe, and David J Wineland. Architecture for a large-scale ion-trap quantum computer. *Nature*, 417(6890):709–711, 2002.

[60] H Ch NAÈgerl, D Leibfried, H Rohde, G Thalhammer, J Eschner, F Schmidt-Kaler, and R Blatt. Laser addressing of individual ions in a linear ion trap. *Physical Review A*, 60(1):145, 1999.

[61] Sabine Wölk and Christof Wunderlich. Quantum dynamics of trapped ions in a dynamic field gradient using dressed states. *arXiv preprint arXiv:1606.04821*, 2016.

Eidgenössische Technische Hochschule Zürich
Swiss Federal Institute of Technology Zurich

Declaration of originality

The signed declaration of originality is a component of every semester paper, Bachelor's thesis, Master's thesis and any other degree paper undertaken during the course of studies, including the respective electronic versions.

Lecturers may also require a declaration of originality for other written papers compiled for their courses.

I hereby confirm that I am the sole author of the written work here enclosed and that I have compiled it in my own words. Parts excepted are corrections of form and content by the supervisor.

Title of work (in block letters):

Authored by (in block letters):
For papers written by groups the names of all authors are required.

Name(s):	**First name(s):**

With my signature I confirm that
- I have committed none of the forms of plagiarism described in the 'Citation etiquette' information sheet.
- I have documented all methods, data and processes truthfully.
- I have not manipulated any data.
- I have mentioned all persons who were significant facilitators of the work.

I am aware that the work may be screened electronically for plagiarism.

Place, date	**Signature(s)**

For papers written by groups the names of all authors are required. Their signatures collectively guarantee the entire content of the written paper.